earth

MDPI

Article

Variability and Trends in Ozone and Ozone-Related Stratospheric Trace Gases over St. Petersburg (Russia)

Yana Virolainen [1,2,*], Alexander Polyakov [1,2], Svetlana Akishina [1], Dmitry Ionov [2], Peter Nerobelov [1], Eugene Rozanov [1,3,†], Vladimir Zubov [1,4], Oliver Kirner [5] and Georgy Nerobelov [1,*]

[1] Ozone Layer and the Upper Atmosphere Research Laboratory, St. Petersburg State University, 199034 Saint Petersburg, Russia; a.v.polyakov@spbu.ru (A.P.); s.akishina@spbu.ru (S.A.); peter_nerobelov@mail.ru (P.N.); v_zubov@rambler.ru (V.Z.)
[2] Physics of Atmosphere Department, St. Petersburg State University, 199034 Saint Petersburg, Russia; d.ionov@spbu.ru
[3] Physical Meteorological Observatory and World Radiation Centre, CH-7260 Davos, Switzerland
[4] Voeikov Main Geophysical Observatory, 194021 Saint Petersburg, Russia
[5] Scientific Computing Center, Karlsruhe Institute of Technology, 76131 Karlsruhe, Germany; ole.kirner@kit.edu
* Correspondence: yana.virolainen@spbu.ru (Y.V.); akulishe95@mail.ru (G.N.)
† Deceased author.

Abstract

Anomalous ozone loss in the Northern Hemisphere during winter–spring periods has been increasingly observed in recent decades. Regular monitoring of stratospheric gases involved in ozone-depleting processes is essential for predicting the appearance of ozone mini-holes and the growth in UV surface irradiance. The St. Petersburg State University site located on the border of mid- and high latitudes is equipped with the Bruker IFS 125HR spectrometer for trace gas measurements and the UV and VIS Ocean Optics HR4000 spectrometers for total ozone column (TOC) measurements. The harmonization of TOC series from three instruments made it possible to analyze TOC variability during rapid changes in air masses. A decrease in ozone in the 8–18 km ($-0.41 \pm 0.33\%$ yr^{-1}) and 18–25 km ($-0.17 \pm 0.15\%$ yr^{-1}) layers, as well as in stratospheric HNO_3 ($-0.31 \pm 0.18\%$ yr^{-1}), is observed for the 2009–2026 period, along with an increase in HF ($+0.41 \pm 0.20\%$ yr^{-1}) mainly due to changes in atmospheric dynamics over the past decade. An observed decrease in CCl_3F ($-0.43 \pm 0.06\%$ yr^{-1}), CCl_2F_2 ($-0.71 \pm 0.04\%$ yr^{-1}), $ClONO_2$ ($-1.14 \pm 0.82\%$ yr^{-1}), and HCl ($-0.31 \pm 0.16\%$ yr^{-1}) indicates a decrease in the chlorine-containing gases in the atmosphere. A comparison of the EMAC and SOCOLv3 simulations with observations for the common 2009–2019 period showed that ozone variability, including trends, seasonal variations, and rapid winter–spring changes, is described by the models within the measurement uncertainty limits, whereas for HCl, $ClONO_2$, and HNO_3, the quantitative discrepancy between the simulations and measurements exceeds the corresponding measurement uncertainty.

Keywords: atmospheric ozone; ozone-related gases; numerical modeling; EMAC; SOCOLv3; ozone monitoring; FTIR

Check for updates

Academic Editor: Carmine Serio

Received: 21 July 2026
Revised: 28 September 2026
Accepted: 5 October 2026
Published: 10 October 2026

Copyright: © 2026 by the authors. Licensee MDPI, Basel, Switzerland. This article is an open access article distributed under the terms and conditions of the Creative Commons Attribution (CC BY) license.

1. Introduction

Ozone is a natural component of the Earth's atmosphere, as it is formed in chemical reactions from oxygen and other substances under the influence of solar radiation. Stratospheric ozone is vital for the biosphere as it protects flora and fauna from the harmful

biological effects of solar UV radiation [1,2]. The ozone layer completely blocks UV-C solar radiation at wavelengths of 200–290 nm (the Hartley band). Excess solar UV-B radiation in the 290–320 nm wavelength range (Huggins band) is absorbed by biological molecules. This leads to the breaking of chemical bonds and the formation of free radicals that react with each other and with undamaged cells. This, in turn, causes changes in cell properties, cell death, and damage to the body as a whole [3]. Ozone absorbs UV-B radiation in the same spectral range as DNA molecules; therefore, when stratospheric ozone content decreases, more solar UV radiation passes through the atmosphere and is absorbed by DNA molecules in living organisms. A 1% decrease in stratospheric ozone leads to a 2% increase in UV-B radiation reaching the Earth's surface [4]. Anomalies in stratospheric ozone content significantly impact surface UV irradiance and stratospheric radiation. As the Sun rises higher in the sky, the amount of UV radiation reaching the surface increases due to an increase in the effects of multiple scattering and a decrease in the absorption of scattered radiation by ozone [5].

In the 20th century, the increased impact of human activities has led to the pollution of the atmosphere with chemically active gases that destroy stratospheric ozone (e.g., halogen-containing gases) [6,7]. During the 1960s, growing scientific interest in the potential effects of high-altitude aircraft emissions on the stratosphere and ozone layer accompanied the development of research on stratospheric ozone chemistry [8]. In 1970, P. Crutzen proposed the nitrogen oxide (NOx) catalytic cycle as an important mechanism of stratospheric ozone destruction [9], providing a theoretical basis for subsequent investigations of anthropogenic perturbations of stratospheric ozone. This mechanism was subsequently applied to the potential effects of NOx emissions from supersonic aircraft by H. Johnston [10]. In 1974, R. Stolarski and R. Cicerone proposed a chlorine catalytic cycle for ozone destruction [11], while M. Molina and F. S. Rowland proposed that anthropogenic chlorofluorocarbons (CFCs) could lead to stratospheric ozone depletion through chlorine atom-catalyzed reactions [12].

Anthropogenic CFCs are long-lived in the atmosphere, with lifetimes varying substantially among individual species and depending on their chemical loss and atmospheric transport; many have atmospheric lifetimes ranging from decades to centuries [13]. Since they began accumulating in the atmosphere in the 1920s and 1930s [14], during tropospheric transport, CFCs released in different emission regions are gradually transported toward the tropics on timescales of approximately weeks. There, they are transported to the tropopause by rapid convective currents within hours and then rise to the upper layers of the stratosphere through slow diffusion over a period of years. When CFCs enter the stratosphere, they release active chlorine under the influence of solar radiation, destroying ozone molecules in the process [4]. Even though the Montreal Protocol led to a decline in ozone-depleting substances, the observed total ozone behavior from 1998 to 2016, when integrated over the latitude band between 60° N and 60° S, does not robustly demonstrate explicit signs of ozone layer recovery due to the negative trend in observed ozone content in the lower stratosphere [15]. Despite the phase-out of production of gases such as CCl_3F (CFC-11) and CCl_2F_2 (CFC-12), continuing industrial emissions of some ozone-depleting substances have been reported and may delay stratospheric ozone recovery [16,17].

Stratospheric gases such as HCl, $ClONO_2$ and HNO_3 are reservoirs for active compounds and radicals. Under certain conditions, they undergo chemical and photochemical reactions that result in chains of reactions destroying ozone molecules [18,19]. The increase in the atmospheric content of chlorine-containing gases in recent decades is a consequence of long-term CFC emissions. Conversely, a decrease in the concentration of these gases will indicate a reduction in ozone destruction caused by anthropogenic activity in chlorine cycles. This is particularly relevant for mid- and high-latitude regions that are affected by

the polar stratospheric vortex (PSV), whose evolution in the Northern Hemisphere exhibits substantial interannual variability [20].

The main destruction of stratospheric ozone occurs within the PSV, which is an area of strong circular winds that forms in late autumn. This isolates the air mass inside the vortex, keeping it in a very cold state. The extent of polar ozone depletion is closely related to stratospheric temperature, which influences the formation of polar stratospheric clouds (PSC). Heterogeneous chemical reactions then occur on the surface of these clouds, leading to the subsequent destruction of ozone in polar latitudes in early spring [21]. When sunlight appears in spring, the low temperature of the lower stratosphere causes air masses to move upwards, carrying ozone-depleted air from the lower layers into the stratosphere and contributing to the rapid destruction of ozone at high altitudes. Once the PSV has been destroyed, polar air can mix with air from the mid-latitudes, which can also lead to a decrease in stratospheric ozone content in these regions [22].

In recent decades, there has been an episodic decrease in total ozone content during the winter and spring in the Northern Hemisphere [23–25], which is smaller than the Antarctic ozone hole in terms of both time and space [26], but it also has negative consequences for humans because it is often observed near densely populated areas of the Northern Hemisphere. Recent observations over St. Petersburg and Northwestern Russia during the March 2025 low-ozone episode further demonstrate the importance of dynamical processes, although chemical ozone loss also contributed to the anomaly [27].

The impact of climate and environmental conditions on human life highlights the need for humanity to adapt to observed changes, particularly the requirement for reliable forecasts of future changes. Modern numerical chemical climate models (CCMs) have the potential to consider all the factors and processes that influence climate and gas composition. However, the results of predictions of future changes by different CCMs vary significantly [28]. To adequately understand and describe the mechanisms of ozone destruction and predict changes to the ozone layer by modern CCMs, it is necessary to monitor not only ozone, but also the related gases that participate in ozone cycles and influence dynamical and chemical processes that lead to increased variability and decreased ozone content during the winter and spring [2]. The validation of CCMs through the comparison with experimental data is one of the most important steps in model development [29].

Because surface UV irradiance can increase during ozone anomalies, the analysis of the formation of these anomalies is especially relevant in areas of high-latitude densely populated megacities. Ground-based Fourier transform infrared (FTIR) measurements of solar radiation transmitted through the atmosphere can be used to investigate the variability of stratospheric gases with high temporal resolution. Within the NDACC (Network for the Detection of Atmospheric Composition Change) framework, observational sites around the globe, equipped with high-spectral-resolution FTIR spectrometers, provide long-term ground-based measurements of atmospheric composition that are used for monitoring atmospheric variability and for satellite and model validation [30,31]. The St. Petersburg site (59°53′ N, 29°50′ E, 20 m a.s.l.), located near the mid-to-high latitude border, is equipped with the Bruker IFS 125 HR spectrometer certified by the Infrared Working Group (IRWG) of the NDACC network [32]. Its unique location allows variations in stratospheric gases to be observed under various atmospheric conditions, including PSV intrusion. The trace gas ozone and ozone-related species (HNO_3, $ClONO_2$, HCl and HF) are required by the IRWG to be measured at NDACC IRWG sites [33]. CFC-11 and CFC-12 are additionally measured at the site to control the effectiveness of fulfillment of the Montreal Protocol and its amendments and adjustments. The atmospheric content of HF is considered as an indicator of dynamic processes in the stratosphere [34]. Analysis of its variability, together with analysis of the variability of chemically active stratospheric gases, enables

the distinction between chemical and dynamic causes of changes in ozone content [35]. Previous studies at the St. Petersburg State University (SPbU) observational site (see, for example, refs. [32,36–38] provided the methodological and observational basis for the present work. The present study extends this research by providing an integrated analysis of ozone and multiple ozone-related stratospheric trace gases over the extended June 2009–May 2026 observational period, combining FTIR and harmonized UV/VIS DOAS total ozone measurements with evaluation of EMAC and SOCOLv3 simulations. In addition to long-term trends, we consider seasonal variability, rapid intraday ozone changes, and individual episodes of enhanced stratospheric variability.

A recent study by Virolainen et al. [39] examined the spatial and temporal variability of total and tropospheric ozone over Russia using satellite observations and numerical modeling, including SOCOLv3. That study provided a regional-scale assessment of ozone variability over Russia, whereas the present study focuses on long-term ground-based FTIR observations at the St. Petersburg State University (SPbU) site, provides a detailed analysis of ozone and ozone-related trace gases, and assesses the quality of modeling data and areas of possible use of CCMs for describing and predicting the variability of atmospheric ozone at various temporal scales.

2. Materials and Methods

2.1. FTIR Measurements of Ozone and Ozone-Related Gases

The Bruker IFS 125HR spectrometer is part of the scientific facilities of the SPbU Resource Center "Geomodel". The instrument is equipped with MCT (mercury cadmium telluride) and InSb (indium antimonide) detectors, enabling measurements of direct solar radiation passing through the atmosphere in the IR region (650–5400 cm^{-1}) with ultra-high spectral resolution (0.01–0.002 cm^{-1}) [40]. Regular spectral measurements were initiated at the SPbU observational site in Peterhof (30 km west of the St. Petersburg center) in 2009 [32]. The FTIR observational record considered in this study extends from June 2009 to May 2026. Due to the climate and weather conditions, and the varying length of daylight hours in different seasons, the temporal sampling is uneven, and the average number of measurement days is approximately 70 per year, predominantly occurring in spring and summer. Instrumental problems caused additional gaps in the observational record, including the absence of FTIR observations in 2020, 2021, and 2024.

2.1.1. Main Features of Trace Gas Retrieval Procedure

We analyzed spectra with the PROFFIT96 (for O_3, HNO_3, $ClONO_2$, and ClO) and SFIT4 (for CFC-11, CFC-12, HCl and HF) software routinely used at the NDACC IRWG sites [41].

When processing the spectra, the pressure and temperature profiles were specified for each measurement day (12 UTC) using NCEP CPC (Climate Prediction Center of the National Centers for Environmental Prediction) reanalysis data, based on satellite and radiosonde measurements and provided by the NDACC IRWG community [33]. The a priori concentration profiles of atmospheric gases affecting radiative transfer in the relevant spectral regions were taken from existing WACCM v.7 (Whole Atmosphere Community Climate Model) model output [42]. Specifically, 40-year mean concentration profiles for 1980–2020 were used. These profiles were prepared for the NDACC IRWG observational stations and provided within the framework of the harmonization of FTIR retrieval strategies across the NDACC network. No individual WACCM simulations were performed for the present study. The HITRAN2020 database [43] (HIgh-resolution TRANsmission) was used to determine the parameters of the fine structure of the absorption bands of atmospheric gases. Other details of the retrieval strategies applied can be found

in references [36,38,44–46]. Time series of total column (TC) measurements of stratospheric gases have been routinely used to validate various satellite data and to compare with the results of numerical modeling (see, for example, refs. [32,37,46,47]).

Table 1 presents some statistical characteristics of trace gas retrieval at the St. Petersburg site—the number of degrees of freedom for the signal (dofs), which indicates the number of independent pieces of information derived from the spectral measurements [48], and statistical (random) and systematic errors. For $ClONO_2$, CFC-11, and CFC-12, it is possible to retrieve only TCs, whereas for HCl, HF, HNO_3, and O_3, the vertical structure can be derived from FTIR spectra.

Table 1. Statistics of the FTIR retrieval for TCs of ozone-related gases at the SPbU site in 2009–2026: N—number of measurement days, dofs—degrees of freedom for signal, Error st—statistical (random) error, Error sys—systematic error (means ± standard deviation).

Target Gas	N	Dofs	Error st, %	Error sys, %	Reference
O_3	957	4.3 ± 0.3	2.2 ± 0.6	3.0 ± 0.5	[37]
HNO_3	894	3.1 ± 0.4	4.0 ± 2.1	9.3 ± 1.7	[37]
$ClONO_2$	837	1.02 ± 0.07	22 ± 9	28 ± 8	[37]
HCl	1006	2.5 ± 0.2	2.1 ± 0.6	5.2 ± 0.1	[38]
HF	1076	2.6 ± 0.3	2.2 ± 0.6	5.6 ± 0.1	[38]
CFC-11	908	1.05 ± 0.06	3.23 ± 0.77	7.60 ± 0.18	[36]
CFC-12	595	1.20 ± 0.05	2.56 ± 0.94	2.26 ± 0.16	[36]

The retrieval uncertainties were evaluated using the error-budget approach implemented in the corresponding FTIR retrieval procedures, following the framework described by Rodgers [48]. The random (statistical) uncertainty accounts primarily for measurement noise and other random uncertainties in atmospheric input and retrieval parameters, whereas the systematic uncertainty represents uncertainties in spectroscopic and forward-model/input parameters, including temperature and other atmospheric profiles and instrumental/retrieval parameters. The total random and systematic uncertainties reported in Table 1 were obtained from the corresponding error budgets of the established retrieval strategies for the individual trace gases; the values for each gas are taken from the corresponding retrieval studies indicated in Table 1.

In the frame of NDACC IRWG activity, special tests for O_3 and $ClONO_2$ retrievals have been performed to develop uniform retrieval strategies for all NDACC IRWG observational sites. The strategies were compared using prior information on the concentration profiles of various gases affecting radiation transport in the relevant spectral region, derived from WACCM numerical model versions v.6 and v.7 [42], and the fine-structure parameters of atmospheric gas absorption bands, taken from the HITRAN2008 [49] and HITRAN2020 [43] databases.

The following key conclusions were yielded by a comparison of various strategies:

1. Using the HITRAN2020 database improves the internal quality and consistency of TOC estimates obtained by the ground-based FTIR method. The discrepancy between the calculated and measured radiation is smaller, and dofs value relative to ozone is greater.
2. The total ozone columns (TOCs) obtained using the HITRAN2020 database are less biased in relation to reference measurements made using a Dobson spectrophotometer than those obtained using the HITRAN2008 database (1.6–1.7% versus 3.7%).
3. On average, the tropospheric ozone columns (TrOCs) obtained using the HITRAN2008 database are 2.2% higher than those obtained using the HITRAN2020 database.
4. TrOCs obtained using prior information from the WACCM6 database overestimate the corresponding values obtained using the WACCM7 database by 4.1%. There is a

strong seasonal cycle in the differences, with values up to 25% higher in summer and up to −35% lower in winter relative to the average.

5. On average, $ClONO_2$ TCs calculated using HITRAN2020 are 13% higher than those calculated using HITRAN2008. These differences exhibit a strong seasonal cycle, reaching 40–50% in summer and decreasing to near-zero values in winter.
6. $ClONO_2$ TCs from WACCM6 are approximately 1% higher than those from WACCM7.
7. Based on the internal output parameters of the $ClONO_2$ estimation schemes (discrepancy, dofs and estimation errors), there is virtually no difference between them.
8. Compared to WACCM6, WACCM7 more accurately reflects seasonal variations in $ClONO_2$ TCs at high-latitude NDACC stations.

2.1.2. Estimates of the Possibility of ClO Retrieval

As mentioned previously, chlorine-containing gases play a significant role in the catalytic destruction of ozone. The amount of ozone destroyed in reactions involving chlorine compounds depends on the concentrations of ozone and active (ozone-depleting) radicals, such as atomic chlorine (Cl) and chlorine oxide (ClO). These concentrations are influenced by stratospheric temperature, solar radiation, and the concentrations of inert reservoir gases, such as $ClONO_2$ and HCl [21]. Understanding the processes associated with ozone layer depletion requires regularly monitoring the atmospheric content of both chlorine radicals and their reservoirs, which do not directly destroy ozone molecules. Since the ClO absorption band falls within the 650–1400 cm^{-1} spectral range, we attempted to determine the feasibility of using FTIR spectral measurements with PROFFIT96 software to assess ClO TCs [41]. We acknowledge that the ClO absorption band is weak compared to other gas absorption bands and that random errors in spectral measurements make it difficult to detect this gas. Therefore, we evaluated the possibility of detecting ClO only during the period of its maximum concentration, which occurs when the PSV enters the atmosphere over St. Petersburg [35].

The spectra were analyzed in seven micro-windows (819.261111–819.550000, 822.0–822.7, 823.55–823.80, 829.15–829.40, 830.400000–830.811111, 831.8–832.1, and 833.2–833.6) among nine gases that absorb in these micro-windows: H_2O, CO_2, O_3, NH_3, HNO_3, OCS, C_2H_6, $ClONO_2$, and CFC-11, CFC-12, and HCFC-22. ClO was also analyzed simultaneously, and Tikhonov–Phillips regularization was used. Ozone and C_2H_6 profiles were refined by scaling the prior profile. Profiles of the other influencing gases were taken from the WACCM v.7 database.

To make a preliminary assessment of the feasibility of retrieving ClO, we used available spectral measurements from November to April of each year starting in 2016. This is when a standard filter was installed at the Bruker IFS 125HR spectrometer, the same filter used in similar instruments at other stations in the IRWG-NDACC observational network. Prior to 2016, the filter introduced quasi-harmonic noise into the measured spectra [44]. Given the narrowness of the ClO absorption band, this made it impossible to determine its concentration in the atmosphere.

After processing the spectra, the results were selected based on two criteria: the spectral mismatch in the micro-windows under consideration had to be less than 0.9 to ensure that the signal from ClO absorption exceeded the measurement noise, and the informativeness of the measurements had to exceed 0.9 so that the ClO TCs could be determined from the spectral data. The average relative retrieval uncertainty of the accepted ClO TC estimates was approximately 70%. This uncertainty characterizes the precision of the retrieved values and should not be interpreted as a formal detection limit. Because the ClO absorption features are weak, reliable retrievals were accepted only when the spectral mismatch and information-content criteria were satisfied. Under the available

measurement conditions in the vicinity of St. Petersburg, reliable ClO retrievals were therefore mainly limited to periods of enhanced ClO abundance during late winter and early spring.

During the winter and early spring, the number of spectral measurements at the SPbU site in Peterhof is very low. This is due to the Sun's low elevation above the horizon, which causes interference from the surrounding forests, and the weather conditions typical of St. Petersburg in winter, such as cyclonic activity. In the presence of cloud cover, it is impossible to measure direct solar radiation. Based on FTIR measurements, periods of PSV entry into the atmosphere over the territory of St. Petersburg were observed only in 2016 [35] and 2023 [38].

Based on FTIR measurements, periods of polar stratospheric vortex influence over the St. Petersburg region were identified in 2016 and 2023 [35,38]. The year 2023 was selected for detailed analysis because suitable FTIR observations of ClO were available during an episode of enhanced ClO associated with PSV-affected air masses. Figure 1 shows the time series of ClO and ozone columns (TCs) obtained from FTIR measurements in early 2023.

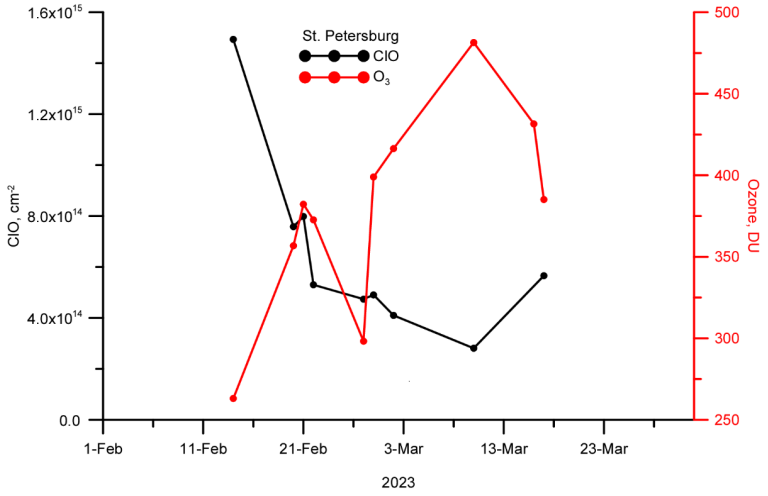


Figure 1. Time series of ClO and ozone TCs obtained from the FTIR measurements at the SPbU observational station in Peterhof in 2023.

The time series of ClO and O_3 total columns obtained from the FTIR measurements in 2023 show an apparent out-of-phase behavior, with enhanced ClO associated with reduced O_3 total columns. This relationship is consistent with the expected role of activated chlorine in polar ozone depletion; however, the observed anti-correlation alone cannot be used to distinguish chemical ozone loss from variations associated with atmospheric transport and dynamics. Therefore, the observed relationship should be regarded as an indication of a possible connection between enhanced ClO and reduced O_3, rather than as direct evidence of chlorine-induced ozone destruction. Additional tracers and dynamical diagnostics are required for quantitative attribution.

The key conclusions from the preliminary analysis of the feasibility of determining ClO TCs from spectral measurements taken with the Bruker IFS 125HR spectrometer at the SPbU site in Peterhof are as follows:

1. Initial calculations showed that due to the low absorption intensity in the ClO lines, the ClO TCs can potentially be determined only during peak periods, such as in winter and early spring, when air masses affected by the PSV chemistry enter St. Petersburg's territory, causing the ClO concentration to increase by an order of magnitude. In other periods, ClO TCs in the atmosphere over St. Petersburg are less than their measurement errors.

2. Due to the low altitude of the sun above the horizon and cyclonic activity (cloud cover) in winter, the number of measurements taken at the SPbU site is low. Therefore, it is difficult to track the temporal variability of ClO over St. Petersburg using this method due to the small number of measurements.

2.2. Harmonization of Ozone Ground-Based Measurements

Since 2009, regular TOC measurements have been carried out at the SPbU observational site using Ocean Optics' HR4000VIS and HR4000UV spectrometers. These spectrometers are equipped with a holographic diffraction grating to disperse the light and a multi-element CCD-type photodetector with 3648 elements. These instruments use the DOAS (differential optical absorption spectroscopy) method, which is based on measuring scattered solar radiation spectra in the ultraviolet (UV) and visible (VIS) regions of the spectrum. During analysis, the difference between the measured and calculated optical thicknesses in the absorption band of the gas under study is minimized. Ozone absorption coefficients, extra-atmospheric radiation, and the effective air mass of the atmosphere are used as prior information. The technique for processing spectral data and obtaining TOCs is described in detail in [50]. The UV instrument's spectral measurement range is 280–420 nm, with a spectral resolution of 0.3 nm and a TOC measurement error of 4–5%. The VIS instrument's spectral range is 400–610 nm with a resolution of 0.6 nm, and the TOC measurement error is also 4–5%.

DOAS measurements complement FTIR measurements when analyzing intraday TOC variability because they are performed at low sun elevation (UV) or at sunrise and sunset (VIS), when FTIR measurements are unavailable. Therefore, on certain days, it is possible to track ozone variability during sudden changes in air masses that may not be recorded by each instrument separately. Before studying intraday TOC variability based on FTIR and DOAS measurements, the TOC measurements obtained by both methods must be calibrated to eliminate or reduce systematic discrepancies associated with peculiarities in spectral measurements, instruments, and interpretation methods, as well as parameters of the fine structure of absorption bands in different spectral regions. The analyzed VIS measurements were obtained by averaging all measurements in the range of solar zenith angles (SZAs) of 90–91°, and the UV measurements were taken in the range of SZAs of 70–80°. FTIR measurements were taken during the day for SZAs less than 85°.

Correction of the UV and VIS TOCs was performed using linear regression (DOAS_corr = DOAS × b + a), separately for each season and each dataset. This seasonal separation was necessary because the mean differences between the DOAS and FTIR measurements vary across seasons due to different SZAs and sun azimuths (which affect the paths observed by the instruments), as well as differing measurement errors. Depending on the season, the FTIR method scans an area within a range of 25–150 km; the UV DOAS method covers 100–150 km, and the VIS DOAS method covers 300–450 km [51].

Linear regression was applied only to TOC pairs from days where the difference between morning and evening DOAS TOCs did not exceed 20%. These were days with stable ozone distribution fields over St. Petersburg, where the average daily measurements from both methods were consistent with both morning and evening DOAS measurements, and with FTIR measurements taken throughout the day.

Figure 2 shows scatter plots of FTIR and UV and VIS DOAS TOCs for all comparisons, before and after correcting the DOAS measurements. The UV and VIS datasets were processed separately. First, the DOAS TOCs were corrected using linear regression performed separately for each season. After the seasonal regression correction, a 2σ filtering criterion was applied separately to the UV and VIS datasets. Observation pairs for which the residual discrepancy between the corrected DOAS and FTIR TOCs exceeded two

standard deviations of the corresponding dataset were excluded. This criterion corresponds approximately to a 95% confidence interval.

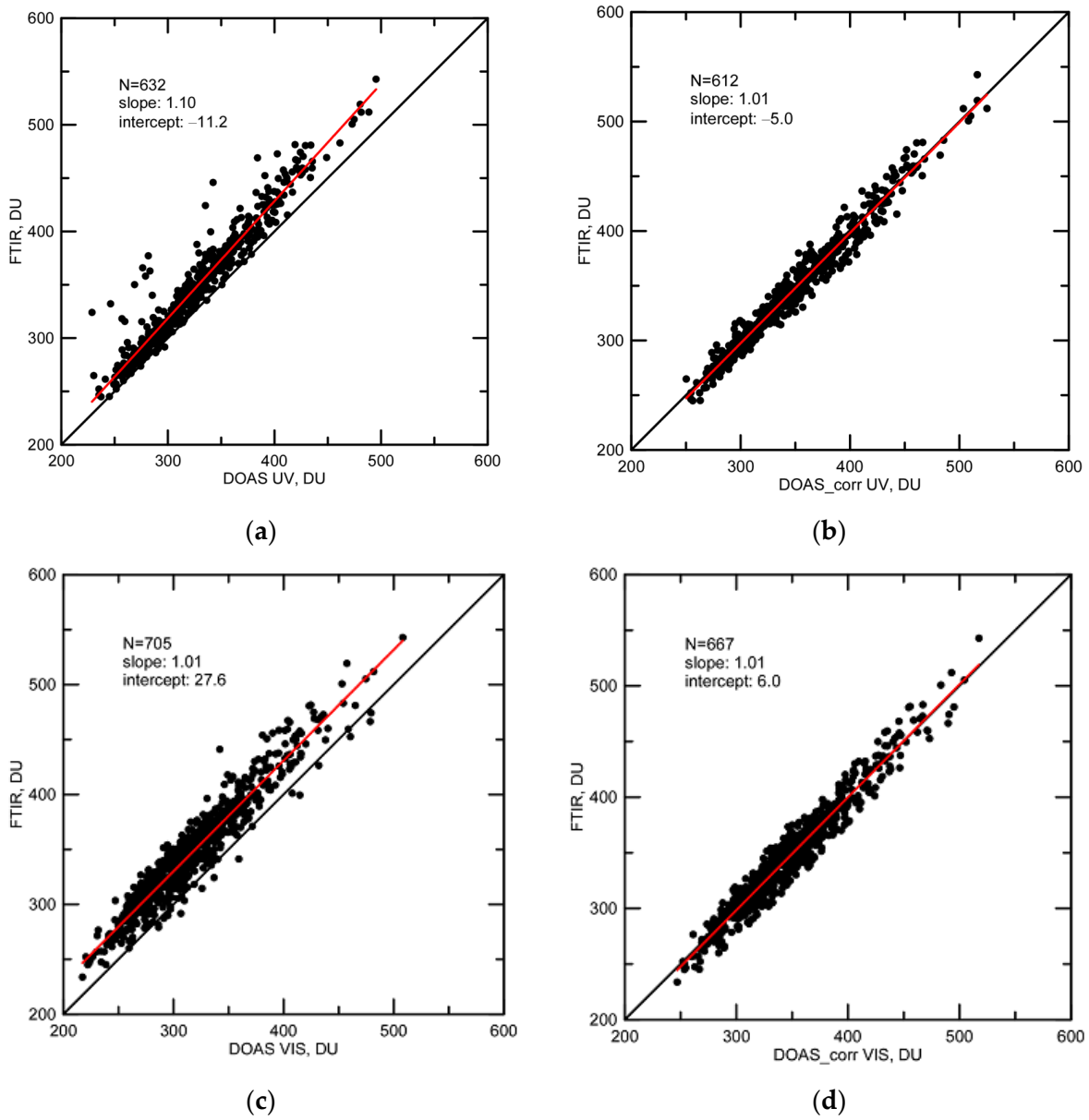


Figure 2. Scatter plots for FTIR and DOAS UV (**a**,**b**) and VIS (**c**,**d**) TOCs before (**a**,**c**) and after (**b**,**d**) correction. The red lines represent linear approximations of the data points.

The number of FTIR–DOAS observation pairs was reduced from 632 to 612 for the UV dataset and from 705 to 667 for the VIS dataset after applying the 2σ filtering criterion (Figure 2). After making these corrections, the TOC datasets were consistent within 2–3%. This enabled us to analyze the intraday variability of TOC using harmonized time series of measurements from the three instruments at the SPbU observational site.

Comparing DOAS measurements with data from the independent Dobson spectrophotometer #108 [47,52] at the Voeikovo station, which is located 50 km northwest of the SPbU site, revealed that data correction improved agreement with TOC reference measurements. The UV measurement bias decreased from −5% to 1.5%, and the standard deviation of differences (SDD) decreased from 3.7% to 2.7%. The VIS measurement bias decreased from −9% to 1%, and the SDD decreased from 4.4% to 3.2%. After correction, the TOC measurement data from all four instruments became consistent within 2–3%. This allowed

for the analysis of intraday TOC variability using harmonized time series of measurements from three instruments.

2.3. Modeling Data

Chemistry-climate models allow us to simulate and predict spatial and temporal variations in trace gases. This study tested the performance of two widely used ozone layer research and prediction models, EMAC and SOCOLv3, against experimental data collected near St. Petersburg.

EMAC and SOCOLv3 were selected because simulations from both models were available for the St. Petersburg observational period and provided sufficient temporal overlap with the FTIR observations for a common-period evaluation. Both models explicitly represent stratospheric chemistry and dynamics and include the trace-gas species required for the present comparison. Their concurrent use also provides an opportunity to assess the sensitivity of the model–observation agreement to different chemistry-climate model formulations.

The EMAC (ECHAM/MESSy Atmospheric Chemistry) model is a numerical chemistry and climate simulation system that includes submodels describing tropospheric and middle atmosphere processes and their interaction with oceans, land and human influences [53]. It combines the ECHAM5 general circulation model [54] with various submodels integrated by the MESSy (Modular Earth Submodel System) interface [55]. EMAC simulates chemical and dynamic processes from the troposphere to the mesosphere (from the surface to 1 Pa or 80 km).

For this study, an EMAC simulation (ECHAM5 version 5.3.02 and MESSy version 2.53) was performed with a horizontal resolution of 2.8° × 2.8° and a vertical resolution of 90 hybrid vertical levels. The simulation results for various gas contents simulated by EMAC are a time series with hourly or eleven-hourly output. CCM incorporates 135 gaseous species and 298 chemical reactions and photolysis, including heterogeneous reactions. The simulation's meteorology was nudged toward ECMWF ERA-Interim reanalysis [56]. The EMAC simulations available for this study cover the period 2002–2019. The extension of the simulations beyond 2019 was not possible because the scientific collaboration required to continue these simulations was discontinued following the interruption of international research cooperation after 2022. Consequently, the model evaluation is restricted to the common observation–model period.

SOCOLv3 CCM (SOlar Climate Ozone Links) [57] consists of MA-ECHAM5 (Middle Atmosphere ECHAM) [58] and a modified MEZON (Model for the Evaluation of oZONe trends) [59] chemistry-transport model. MA-ECHAM5 and MEZON interactively couple via three-dimensional temperature and wind fields as well as the radiation effects of water vapor, ozone, methane, nitrous oxide, and CFCs. MA-ECHAM5 is an extended, comprehensive parameterization package for climate applications of the ECHAM5 model. The MA-ECHAM5 version for the middle atmosphere can be run with 39 or 90 vertical levels. The top of the model is centered at 0.01 hPa (approximately 80 km) for both vertical resolutions. The MEZON includes 41 chemical species of oxygen, hydrogen, nitrogen, carbon, chlorine, and bromine groups, which are determined by 140 gas-phase reactions, 46 photolysis reactions, and 16 heterogeneous reactions in/on aqueous sulfuric acid aerosols, as well as three types of PSCs: supercooled ternary solution droplets, water ice, and nitric acid trihydrate.

For this study, model simulations were conducted at 39 vertical levels using T42 (2.79°) horizontal resolution from 2008 to 2022. The numerical simulations were nudged toward the atmospheric state from ERA5 (ECMWF, European Centre for Medium-Range Weather

Forecasts, ReAnalysis generation 5) meteorological reanalysis [60]. The main features of the current version of the SOCOLv.3 model simulation are presented in [39].

To ensure a consistent direct comparison of both models with the observations, the model–observation evaluation is restricted to the common 2009–2019 period. Extension beyond 2019 is not possible for the two-model comparison because EMAC simulations are not available after 2019.

3. Results and Discussion

3.1. Study of Ozone and Ozone-Related Gases Variability Using the FTIR Method

3.1.1. Measurements of Stratospheric Trace Gases

Time series of ozone and ozone-related gases measured at the SPbU site in 2009–2026 are presented and discussed in Appendix A.1. Here we consider the statistical distribution of TCs of stratospheric gases.

Figure 3 depicts the distribution of daily mean TCs of O_3, HCl, HNO_3, and $ClONO_2$ measured by the FTIR method near St. Petersburg in 2009–2026. Red lines show the lognormal fits of the time series considered. The distribution of TC values is most symmetrical relative to the mean values for HCl, suggesting that the processes causing this gas' variability through the entire period of measurements are stable. For ozone, there is a slight shift toward higher values associated with its increased presence in the spring, which varies from year to year. For nitric acid, the shift toward a smaller number of higher TC values is more pronounced. The distribution peak for $ClONO_2$ occurs at low TC values since chlorine nitrate TCs increase by several orders of magnitude because of photochemical reactions only in the spring. During the rest of the year, background TC values of $ClONO_2$ are often observed; moreover, they can be even smaller than the measurement error of the FTIR method (see Table 1).

The histograms also illustrate the range of variation in stratospheric gas TCs observed near St. Petersburg. HCl and O_3 are the least variable (TC variations vary only by factors of 2 and 2.5, respectively) with nearly symmetrical lognormal distribution of TCs. $ClONO_2$ is the most variable, changing by several orders of magnitude. The TC of HNO_3 varies by a factor of four.

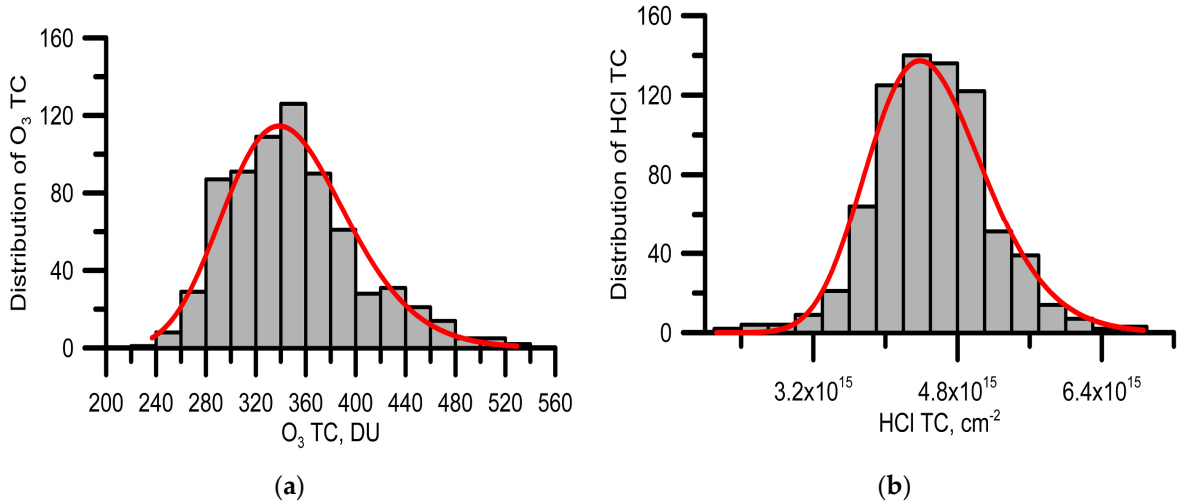


Figure 3. *Cont.*

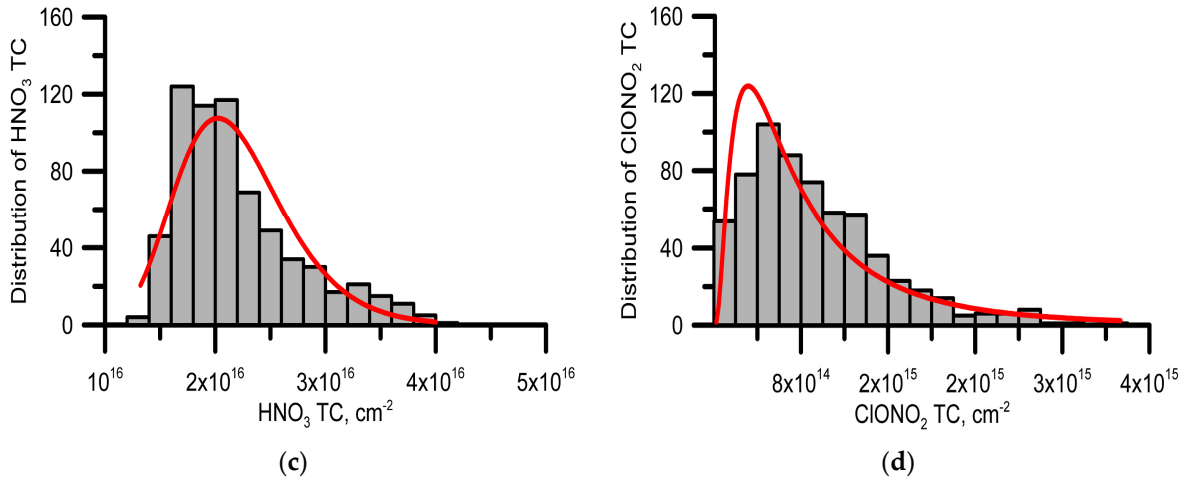


Figure 3. Distribution of daily mean FTIR measurements of O_3 (**a**), HCl (**b**), HNO_3 (**c**), and $ClONO_2$ (**d**) TCs near St. Petersburg in 2009–2026 along with their lognormal fit (red line). The numbers of valid daily mean observations are 957, 1006, 894, and 837 for O_3, HCl, HNO_3, and $ClONO_2$, respectively.

3.1.2. Trend Analysis

The 17-year series of trace gas measurements at the SPbU site (from June 2009 to May 2026) allowed us to assess trends and seasonal variability using the methodology described in [36]. Seasonal variability, which is periodic in nature, is modeled using a Fourier series of several orders that reflects the fundamental periodicity of the data. The methodology's model [61] allows for gaps in the data series without causing discontinuities in the seasonal trend function. This is important for infrared (IR) measurements of direct solar radiation, where the number of measurements per year can be distributed unevenly. The Bootstrap method is used to resample data to estimate confidence interval bounds and determine the statistical significance of trend estimates. This method allows for reliable analysis of data that does not follow a normal distribution, considering that FTIR measurements have systematic (non-random) errors (see Table 1).

As the FTIR observations are unevenly distributed throughout the year, with substantially fewer measurements available in winter than in spring and summer (Table A1), separate seasonal or monthly trend estimates would be associated with considerably larger sampling uncertainty. In particular, winter and monthly trends could be strongly affected by individual years with limited observations or data gaps. We therefore focus the trend analysis on the full observational period, while the seasonal variability is assessed separately using the Fourier-based approach described above. This approach accounts for the periodic seasonal component and accommodates the irregular temporal sampling and gaps in the FTIR time series.

Table 2 shows the estimated trends of ozone and several ozone-related gases during the period when measurements were taken at the SPbU site in Peterhof using the ground-based FTIR method. This period spans from June 2009 to May 2026. Statistically significant estimates at the 95% confidence level are in bold. The seasonal sampling limitations should be considered when interpreting the annual trends, particularly because the strongest dynamical variability occurs during winter and spring. The seasonal characteristics of the observed trace gases are therefore discussed separately in Section 3.1.3.

Estimates of long-term trends in trace gas content may vary depending on the calculation method, time period, or dataset used. In the current study, no significant TOC trend is observed near St. Petersburg by FTIR measurements for the 2009–2026 period, whereas for

2004–2021, a small, statistically significant positive trend of +0.4 DU per year based on a harmonized set of experimental and model data was identified [47].

Table 2. Trend estimates of ozone and ozone-related gases measured in different atmospheric layers at SPbU site by FTIR method from June 2009 to May 2026. Statistically significant estimates at 95% confidence level are in bold.

Target Gas	Layer, km	Trend, % yr^{-1}
O_3	0–60	-0.11 ± 0.13
	0–8	$+0.08 \pm 0.16$
	8–18	$\mathbf{-0.41 \pm 0.33}$
	18–25	$\mathbf{-0.17 \pm 0.15}$
	25–60	$\mathbf{+0.16 \pm 0.12}$
HNO_3	0–60	-0.25 ± 0.25
	0–15	-0.13 ± 0.55
	15–60	$\mathbf{-0.31 \pm 0.18}$
$ClONO_2$	**0–60**	$\mathbf{-1.14 \pm 0.82}$
HCl	**0–60**	$\mathbf{-0.31 \pm 0.16}$
Cly	**0–60**	$\mathbf{-0.48 \pm 0.22}$
HF	**0–60**	$\mathbf{+0.41 \pm 0.20}$

During the period from 2009 to 2026, a statistically significant decrease was observed in O_3 columns in the 8–18 km (lower stratosphere) and less pronounced in 18–25 km (mid-stratosphere) layers. The study [62] reported stratospheric ozone trends in the 60° S–60° N latitude range in 2000–2024 based on merged remote-sensing datasets and chemistry-climate model simulations. They found mostly negative (from −1 to −6 % per decade) but non-significant trends in the lower stratosphere and demonstrated longitudinal structure in the Northern Hemisphere mid-latitude stratosphere with positive trends over Scandinavia and negative trends over Siberia. Ground-based records at individual stations were broadly consistent with the vertical structure identified from the merged datasets. While comparing with the same evaluation of stratospheric ozone trends in 2000–2020, slight changes in trends were detected [62], possibly due to extra-high ozone values observed in the middle and lower stratosphere of the Northern Hemisphere in 2024 associated with high planetary wave activity [63]. It should be noted that there were no FTIR observations at the SPbU site in 2024 due to instrumental problems (see Appendix A.1), which may influence the more pronounced negative trends presented in Table 2 compared to other studies.

A statistically significant decrease is also detected in stratospheric HNO_3 columns. The decreases observed in the lower and mid-stratosphere are most likely caused by changes in atmospheric dynamics in the Northern Hemisphere over the past decades [20,64], including more frequent incursions of polar air masses into mid-latitudes, which have also led to an increase in HF TCs mainly driven by a decrease in tropopause height during these events. An observed increase in HF TCs can also be explained by the long stratospheric lifetime of HF: the only known sink of stratospheric HF is transport to the troposphere followed by rainout and by the fact that fluorine emission is not explicitly restricted [65]. Long-term trends for a number of species measured by the FTIR method in Toronto (Canada) during 2002–2019 were studied in [66]. They found a statistically significant positive trend in HF TCs of $0.59 \pm 0.11\%$ yr^{-1}, which agrees with the results of the current study.

The study [67] examined long-term trends in ozone columns in various atmospheric layers based on ground-based measurement data, including FTIR spectrometers, ozone sondes, and Dobson and Brewer spectrophotometers, in the Arctic and adjacent regions from 2000 to 2024. The obtained trend estimates are mixed and vary across different regions, seasons, and atmospheric layers. They may be statistically significant (positive

or negative) or statistically insignificant. The annual trends indicate a positive evolution of TOCs over the Arctic, which is statistically significant over Canada (+2.1% per decade) and over Northwest Europe (+0.7% per decade). An annual ozone recovery was detected for the Canadian region (+2% per decade) in the mid-stratosphere and for the North Pole region in the upper stratosphere (+2.1% per decade).

Annual tropospheric ozone trends are negative for the North Pole region, but not significant for Scandinavia, which is consistent with the trend estimates of TrOCs in the current study, as the St. Petersburg region can be considered within Scandinavia.

We found no significant trend for HNO_3 TCs, whereas the study [66] detected a positive trend of $0.36 \pm 0.13\%$ yr^{-1}, which can be explained by different stratospheric dynamics over Canada and Eurasia.

In the current study, we also observed statistically significant decreases in the TC values for CFC-11, CFC-12, $ClONO_2$, HCl, and Cly ($ClONO_2$ + HCl), together with an increase in upper-stratospheric O_3. Based on FTIR measurements, our estimates of the decrease in CFCs in the vicinity of St. Petersburg from 2009 to 2025 were $-0.43 \pm 0.06\%$ yr^{-1} and $-0.71 \pm 0.04\%$ yr^{-1} for CFC-11 and CFC-12, respectively.

Our observed decrease in HCl, $ClONO_2$, and Cly is consistent in sign with the long-term decline in atmospheric chlorine reported from ACE-FTS observations. Raymond et al. [68] estimated a decrease in total atmospheric chlorine of $-0.254 \pm 0.009\%$ yr^{-1} for the 60–30° N latitude band over 2004–2024, compared with $-0.26 \pm 0.01\%$ yr^{-1} for the Northern Hemisphere as a whole. Their analysis also showed that the decrease in total chlorine has been slowed in recent years by increasing contributions from HCFCs and chlorine-containing very short-lived substances. The larger negative trend observed for Cly in the present study ($-0.48 \pm 0.22\%$ yr^{-1}) should not be directly interpreted as a quantitative counterpart of the ACE-FTS total-chlorine trend, because the two quantities represent different chlorine reservoirs and are derived using different vertical and spatial sampling.

In [66], HCl showed a decreasing trend of $-0.11 \pm 0.04\%$ yr^{-1}, which is smaller than observed estimates of the current study. This difference can be explained by the different time period for trend estimates: in [66], the years 2002–2019 were covered, and in the current study, the years 2009–2026 were covered. During the 2007–2011 period, an increase in HCl TCs was observed over NDACC sites in the Northern Hemisphere and explained by the atmospheric circulation changes [69]. Recent ACE-FTS observations and chemical-transport modeling further demonstrate that HCl and lower-stratospheric ozone trends exhibit pronounced hemispheric asymmetry and that transport variability can strongly influence these trends, with chemical feedbacks further modifying the ozone response [70]. The study [71] examined trends in inorganic stratospheric chlorine by means of measurements and modeling in both hemispheres; they found that HCl + $ClONO_2$ trends are caused by the combined effect of transport (a slowdown of the Brewer–Dobson circulation in the Northern Hemisphere) and emission changes. They also showed that the long-term reduction in inorganic stratospheric chlorine is partly offset by increasing contributions from chlorinated very short-lived substances. Recent ACE-FTS chlorine inventories provide a complementary observational perspective on the long-term evolution of CFC source gases and inorganic chlorine product gases [70,71].

In [72], it was demonstrated that HNO_3 and HCl TCs are the most sensitive to transport circulation changes in the middle and upper stratosphere; the authors revealed extratropical variability with a 5–7-year period driven by interactions between the circulation and tropical winds. This may influence the trend estimated for these gases depending on the period considered. Based on the analysis of experimental data for the 1994 to 2018 period, they found no significant trend for HCl ($0.10 \pm 0.22\%$ yr^{-1}) and HNO_3 ($0.08 \pm 0.16\%$ yr^{-1}) in the Northern Hemisphere.

In Appendix A.2, we consider the trend estimates of the ratio of trace gas series to HF TCs, which can be useful in the analysis of short-term variability of ozone and ozone-related gases.

3.1.3. Ozone Partial Columns Seasonal Cycle

Using the Bruker IFS 125HR spectrometer to measure solar radiation spectra at ground level makes it possible to retrieve up to four independent parameters for the major ozone isotope. The dofs (see Table 1) for this isotope range from 3.5 to 4.5 depending on the day and measurement conditions (see, for example, [73,74]). Over the entire measurement period at the SPbU site, the ensemble-averaged number of degrees of freedom is 4.4 ± 0.3. In other words, the ozone content in four layers provides the maximum amount of information about the vertical structure of ozone that can be obtained from spectroscopic measurements using this method. When solving the inverse problem, the ozone mixing-ratio profile is first retrieved and subsequently integrated to determine the ozone content in thick atmospheric layers [45]. Since the ground-based FTIR method determines the ozone columns in four atmospheric layers and provides estimates for TOCs, linear trend and seasonal variation estimates were obtained for the ozone content in the 0–8 km tropospheric layer (TrOCs) and in three stratospheric layers: 8–18 km, 18–25 km, and 25–60 km.

Figure 4 shows the seasonal variations (deviation from the mean value) in ozone content in the considered atmospheric layers and TOC and SOC seasonal behavior. The study [45] examined the trends and seasonal patterns of TrOC and surface ozone concentrations (SOCs) during the measurement period from 2009 to 2022. The seasonal patterns of SOCs, TrOCs, and TOCs are similar, peaking in the spring and reaching a minimum in the fall. However, the seasonal pattern of TrOCs lags by approximately one month, and the seasonal pattern of SOCs lags by 1.5 months relative to the seasonal pattern of TOC. This lag in the spring is due to the gradual movement of ozone-rich air from the stratosphere to the troposphere (see, for example, [75,76]), as well as an increase in solar radiation and temperature, which promotes the mixing of tropospheric layers. The maximum deviation from the mean for TOC is approximately +20% in early March and ~−15% in early October. The maximum TrOCs' deviation from the mean occurs in the first half of April (~+16%), while the minimum (~−12% to −14%) is observed from mid-October through the end of December. The maximum variation in SOCs is observed in the second half of April (over 40%), while the minimum occurs from mid-October through mid-January. A secondary maximum deviation from the mean is evident in mid- and late July, with TrOCs at +7–8% and SOCs at 10–12%. This secondary peak may be associated with high surface temperatures, an increase in the height of the atmospheric boundary layer, increased solar insolation, and seasonally varying precursor availability and transport conditions. Previous studies have shown that the relative importance of precursor emissions and meteorological factors for tropospheric ozone varies seasonally in northern mid-latitudes and urban environments [6,77]. These factors promote the formation and accumulation of tropospheric ozone, even at the latitudes of St. Petersburg. Recent studies indicate that, in addition to local meteorological conditions and precursor availability, regional-scale climate variability can modulate seasonal ozone patterns through changes in atmospheric circulation [78]. However, their individual contributions cannot be quantified from the present dataset because local precursor concentrations and emissions were not analyzed.

The lower stratosphere (8–18 km) exhibits a pronounced seasonal variation, characterized by a maximum in early March (with variations of up to 50%) and a minimum in September (with an amplitude of 30%). The same variation occurs in the ozone stratospheric layer, though its amplitude is smaller. This variation is primarily driven by stratospheric transport and dynamics, including the Brewer–Dobson circulation and tropopause variability as

well as synoptic and mesoscale processes. The large amplitude also arises because this layer includes the tropopause region, which is involved in intense stratospheric–tropospheric exchange. The 18–25 km stratospheric layer, which contains the largest amount of ozone among the considered layers, exhibits a smoother seasonal pattern with an amplitude of about 20%. Peaks occur at the end of winter, and troughs occur at the end of summer when the Brewer–Dobson circulation weakens and the inflow of ozone-rich air masses from the tropics decreases [79]. Seasonal variation in ozone columns in the upper stratosphere (25–60 km) is strongly influenced by photochemical ozone formation processes. Therefore, the opposite pattern is observed here, with maximum values occurring around the summer solstice and minimum values around the winter solstice. The amplitude of variation in ozone content in this layer is about 15%. The same seasonal cycle of ozone columns was detected at other NDACC stations over Western Europe [80].

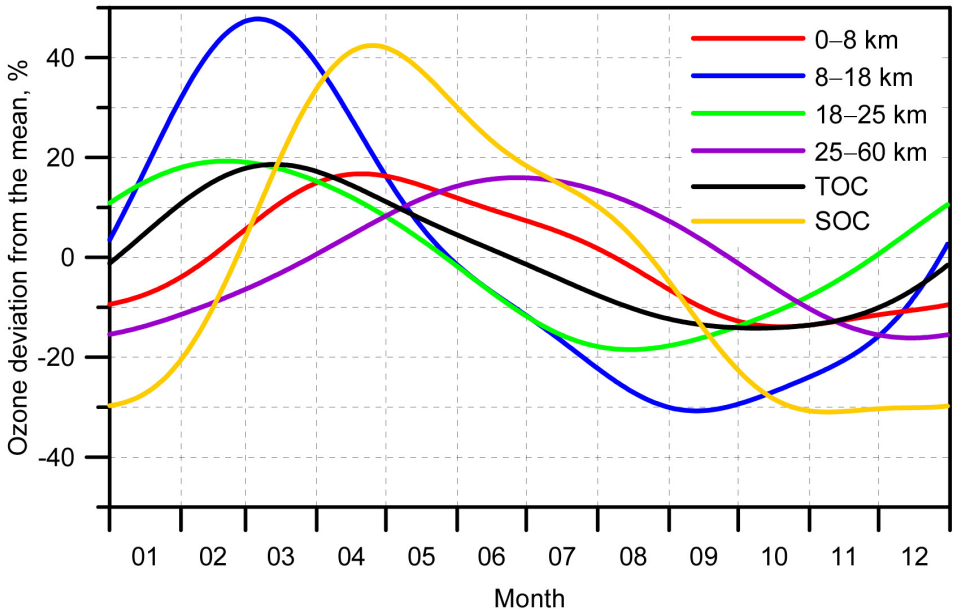


Figure 4. Seasonal cycle of SOC and O_3 in different atmospheric layers obtained by FTIR method near St. Petersburg in 2009–2026.

3.1.4. Case Study of Ozone Intraday Variability

Section 2.2 describes the harmonization of joint TOC measurements using two methods (FTIR and DOAS) and three instruments (Bruker IFS 125HR, OceanOptics UV, and OceanOptics VIS). This harmonization allows the TOC time series to be used for analyzing diurnal variations during periods of high TOC variability.

From the available FTIR TOC measurement time series, days with nine or more measurements and significant diurnal TOC variability observed (the standard deviation of the daily average TOC values exceeded 10 DU) were selected. Then, from these days, those on which both morning and evening DOAS measurements were available in the UV and VIS spectral regions were selected for further analysis. Table 3 presents these days and their respective daily average values and standard deviations (SDs) for FTIR measurements. It also presents the TOCs obtained from UV and VIS measurements in the morning and evening, as well as measurement data from the Dobson spectrophotometer at the reference Voeykovo station (approximately 50 km northeast of the St. Petersburg State University station in Peterhof and east of downtown St. Petersburg) [47]. The Dobson measurements demonstrate the variability of the ozone distribution field in the St. Petersburg region.

Table 3. TOC measurement data for specific days with high ozone variability in the vicinity of St. Petersburg (mean and SD values). The data were obtained using various methods. Am and pm refer to morning and evening DOAS measurements, respectively. For Dobson, the range of variability in available TOC measurements is presented.

Date	FTIR		DOAS UV		DOAS VIS		Dobson
	Mean, DU	SD, DU	am, DU	pm, DU	am, DU	pm, DU	DU
27.03.2013	455.6	11.9	462.1	449.7	476.1	418.9	459–460
23.04.2014	388.7	14.6	374.8	402.8	375.9	400.1	363–382
19.04.2017	425.0	14.1	394.3	448.7	391.6	441.1	384–400
22.02.2019	426.3	22.1	446.2	423.7	478.0	415.1	-
06.03.2019	425.1	21.8	435.2	400.1	439.0	394.8	-
27.03.2019	415.5	51.2	475.5	410.0	512.3	345.9	450–460
03.04.2019	365.4	11.5	328.1	387.2	353.7	411.7	340–374
22.03.2021	459.4	19.7	461.9	453.9	452.4	418.3	-
20.04.2021	375.5	19.1	355.5	400.8	358.2	403.8	366–370

Almost all days fall within the spring period, which is characterized by the greatest day-to-day variability in ozone due to frequent shifts in air masses over St. Petersburg from polar and mid-latitude regions. These regions differ in ozone content due to active chemical processes of ozone formation and destruction during the spring in polar regions. Since satellite measurements are usually taken at each location only once or twice per day, they cannot provide information on diurnal TOC variability. Dobson spectrophotometer measurements do not always reflect ozone variability either, since they are usually taken in direct sunlight over a limited time period. However, combining harmonized DOAS and FTIR measurements makes it possible to track changes in ground-level ozone throughout the day in the vicinity of St. Petersburg.

Table 3 identifies nine days with pronounced diurnal variability in total ozone column. Among these cases, 27 March 2019 was selected for detailed analysis because it exhibited the greatest diurnal TOC variability based on the FTIR measurements. On this day, TOC varied from approximately 512 to 346 DU. The event was selected as an illustrative case study because FTIR, UV and VIS DOAS measurements, together with ERA5 reanalysis data and model simulations, allowed us to investigate the intraday evolution of ozone and the associated air-mass transport. The analysis is intended as a case study of a pronounced short-term variability event rather than as a statistically representative analysis of all high-variability days. Figure 5 provides the TOC distribution fields derived from ERA5 reanalysis data [60] and uses black triangles to highlight the regions from which the SPbU site receives information. The air masses scanned by the instruments are at varying distances and orientations from the ground station depending on the solar elevation angle and azimuth.

For the FTIR method, the region of maximum ozone concentration (at altitudes of 15–25 km) is located at distances of up to 25–150 km. For the UV method, this region is located at distances of up to 100–150 km. For the VIS method, this region is located at distances of up to 300–450 km [51]. Each panel in the figure differs from the previous one by three hours, from (a) to (f). This illustrates how quickly air masses move and how the TOC changes in the vicinity of St. Petersburg. Although reanalysis data based on satellite measurements provide a general qualitative picture of air mass movement, they do not always correspond quantitatively to ground-based measurement data, which can also be used for reanalysis. Using harmonized data from various measurements, particularly different methods for measuring TOCs, makes it possible to analyze diurnal TOC variation. Incorporating data from other gases and reanalysis data enables one to investigate the causes of TOC variability.

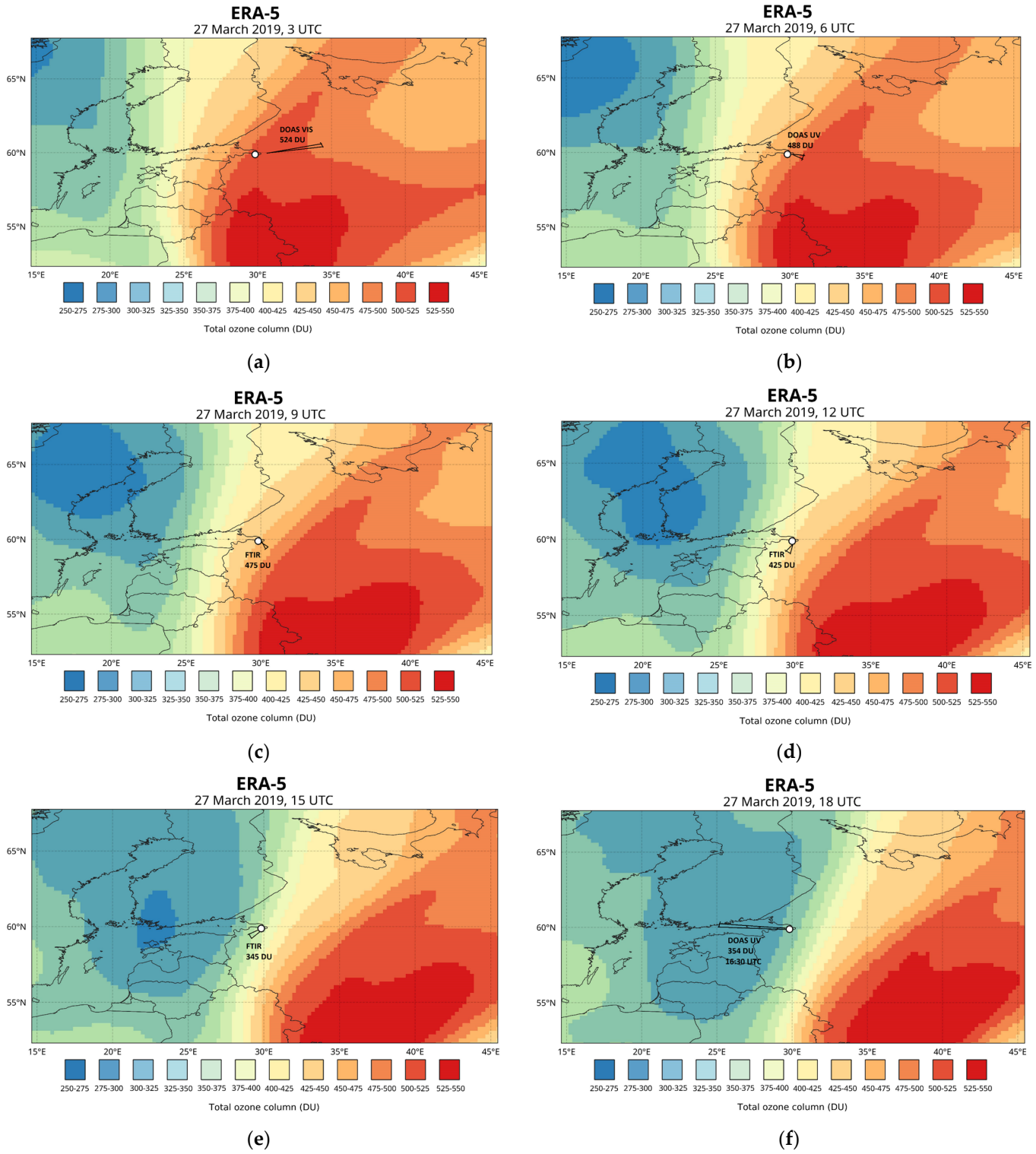


Figure 5. Intraday TOC variations near the St. Petersburg station are based on ERA-5 reanalysis data and ground-based measurements taken at the SPbU site using various instruments on 27 March 2019: (**a**) 3 UTC; (**b**) 6 UTC; (**c**) 9 UTC; (**d**) 12 UTC; (**e**) 15 UTC; (**f**) 18 UTC.

3.2. Evaluation of the Quality of Stratospheric Gas Modeling

The accuracy of the FTIR measurements of O_3, HNO_3, $ClONO_2$, and HCl (see Table 1) meets World Meteorological Organization (WMO) requirements for various atmospheric applications [81]. These measurements allow for the validation of numerical modeling results from the CCM.

Previously, EMAC simulation data had been compared multiple times with ground-based FTIR measurement data at the SPbU observational site in Peterhof. Based on these comparisons, the simulation data were refined. These studies also used earlier versions of the experimental data described in their respective papers. Specifically, the spectral analysis relied on spectroscopic information from the HITRAN2008 database [49] rather than the HITRAN2020 database, which was used in the present study. The EMAC simulation data obtained for 2009–2019, described above, differ from previous calculations; they were performed considering a comparison of models and experiments conducted previously.

3.2.1. Comparison of Trace Gas Time Series: Modeling vs. FTIR Measurements

To make a clear comparison of the two models' calculation results, the time sampling intervals were made identical in accordance with the available data for both models and measurements. The daily average values of the trace gas TCs were used to compare with the simulation data. The simulation data were averaged to daily means to align with the timing of the FTIR measurements. As observational data were obtained only on average 70 days per year, simulated data were taken only on days of measurements; thus, we collected data triplets for each trace gas considered. The resulting numbers of paired daily mean observations were 709 for O_3, 657 for HNO_3, 744 for HCl, and 633 for $ClONO_2$ over the common 2009–2019 period. The same O_3 observation days were used for the comparison of the total and partial ozone columns.

Figures 6 and 7 show the scatter plots of trace gas data pairs FTIR-EMAC and FTIR-SOCOL, respectively, in the vicinity of St. Petersburg between 2009 and 2019. The values of the coefficient of determination, slope, and intercept for each gas are also provided in these figures. Of all the gases considered, the EMAC and SOCOL models show the best agreement with ground-based FTIR measurements of TOC—the data points lie along a diagonal line. The slope of the line compared to FTIR TOC measurements is equal to one for both models. This indicates that both models accurately describe the observed variability of TOC. However, for the EMAC model, the intercept is significantly negative, meaning that the model systematically overestimates the measured data on average. The coefficient of determination for both models is greater than 0.9, indicating that both models accurately reproduce the observed TOC values.

The EMAC-FTIR measurement data pairs for HCl TCs also lie closely along a straight line. However, the slope of this line differs significantly from the diagonal. This indicates that the model underestimates the observed variability of HCl TCs. The coefficient of determination is greater than 0.8. Thus, the EMAC model reproduces the observed HCl TC values well. For the SOCOL model, the points are more widely scattered around the line. The variability of experimental HCl TC at low values roughly corresponds to the model's predictions. At moderate values, however, the model underestimates the variability of HCl TC. The coefficient of determination is approximately 0.6, meaning the model explains more than half of the variability in the experimental data.

The EMAC model better reproduces the variability of HNO_3 and $ClONO_2$ TCs than the SOCOL model. The EMAC model has a coefficient of determination of 0.66 and 0.51 for HNO_3 and $ClONO_2$, respectively. In contrast, the SOCOL model has a coefficient of determination of less than 0.4, meaning it explains less than 40% of the variation in the experimental data. EMAC-FTIR HNO_3 TC data pairs lie close to a straight line. However, the significant intercept suggests that the model systematically overestimates the experimental data overall. The large slope indicates that both models underestimate the observed variability in stratospheric trace gas TCs. It should be noted that for the SOCOL model, the same simulated HNO_3 and $ClONO_2$ TCs may correspond to different measured values. A

similar pattern is observed for the EMAC model and low values of $ClONO_2$ TC. However, this may be due to large measurement errors for this gas in the background range.

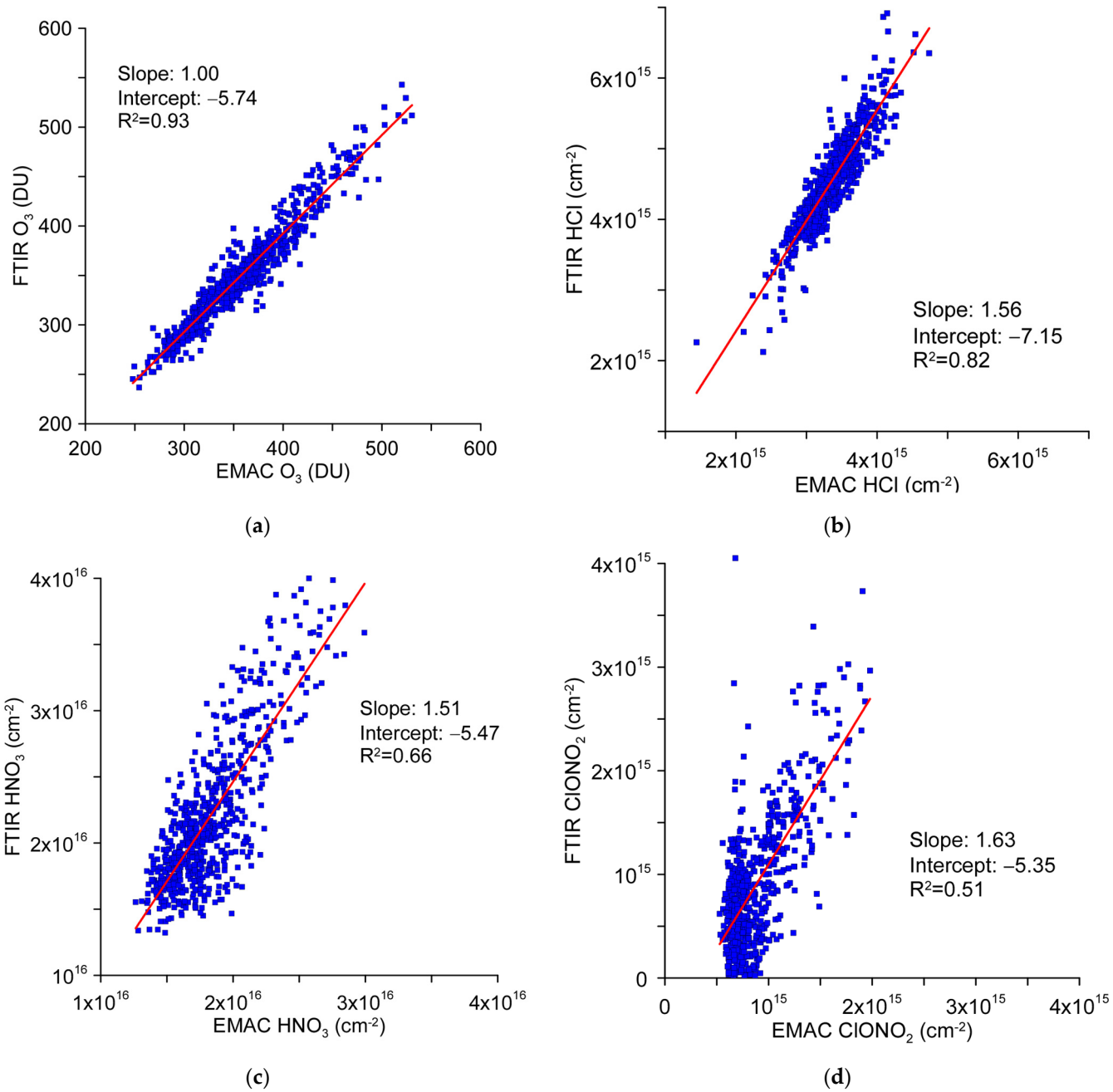


Figure 6. Scatter plots of trace gas total columns: O_3 (**a**), HCl (**b**), HNO_3 (**c**), and $ClONO_2$ (**d**) derived from FTIR measurements and EMAC numerical modeling at the SPbU site in Peterhof from 2009 to 2019. The number of paired daily mean observations is 709 for O_3, 744 for HCl, 657 for HNO_3, and 633 for $ClONO_2$. The red lines represent linear approximations of the data points.

Table 4 summarizes the statistical characteristics of the differences between the FTIR observations and the EMAC and SOCOLv3 simulations. In addition to the correlation coefficient (R), the Willmott index of agreement (d) was used to characterize the overall agreement between modeled and observed values. The two statistics describe different aspects of model performance: R characterizes the consistency of temporal variability, whereas d additionally accounts for the magnitude of deviations between modeled and

observed values and is therefore sensitive to systematic bias and differences in variability amplitude.

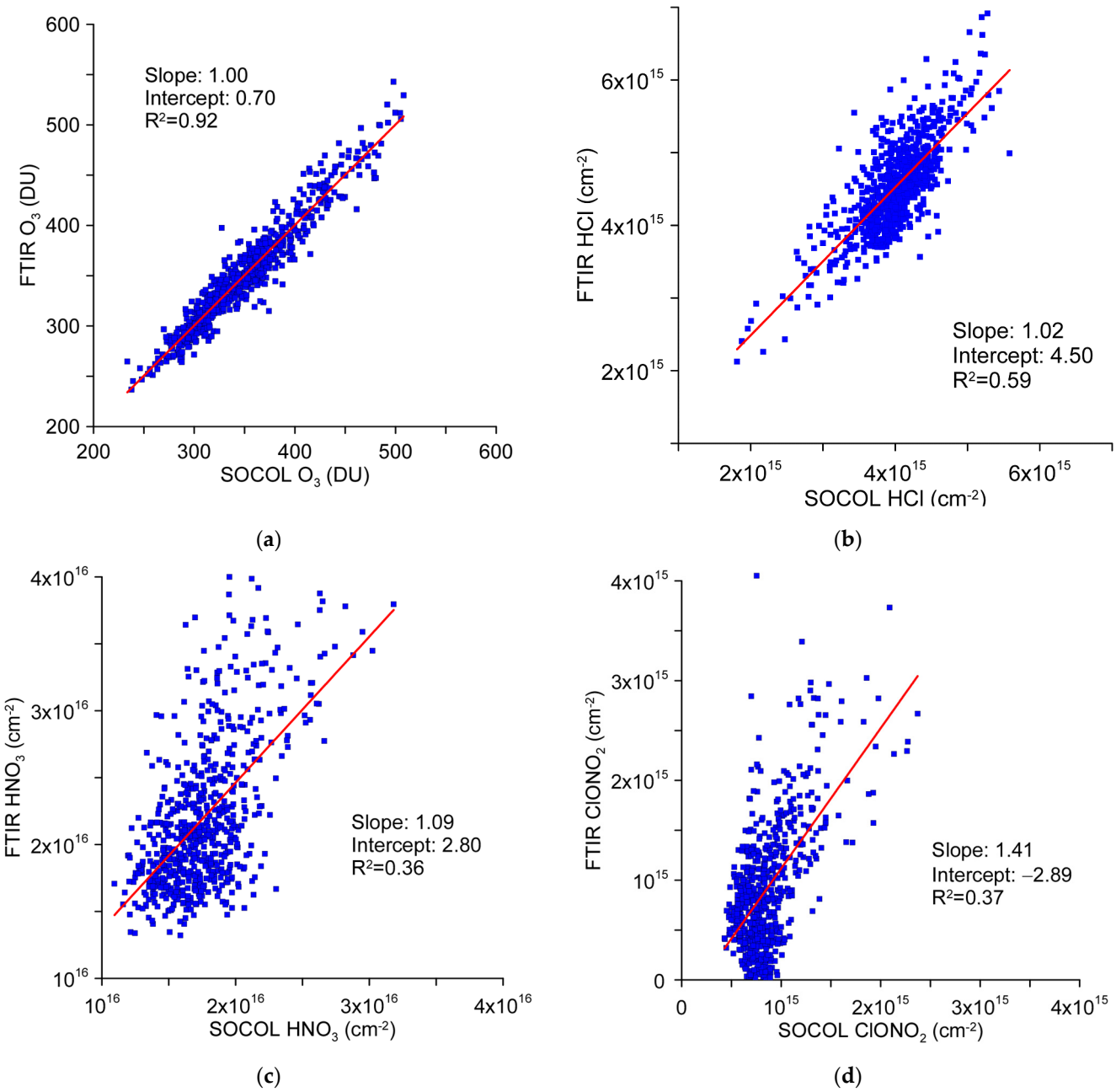


Figure 7. Scatter plots of trace gas total columns: O_3 (**a**), HCl (**b**), HNO_3 (**c**), and $ClONO_2$ (**d**) derived from FTIR measurements and SOCOLv3 numerical modeling at the SPbU site in Peterhof from 2009 to 2019. The number of paired daily mean observations is 709 for O_3, 744 for HCl, 657 for HNO_3, and 633 for $ClONO_2$. The red lines represent linear approximations of the data points.

For TOC, both models demonstrate a high degree of agreement with the FTIR observations, with d equals 0.98 for both EMAC and SOCOLv3. On average, the EMAC model slightly overestimates the measurement data. However, both models are consistent with the TOC measurements within the margin of error of the FTIR measurements. The SDD values are 4–4.3%. Similar consistency is found for the ozone partial columns, although the model performance differs between atmospheric layers.

In the lower stratosphere (8–18 km), the SDD between measured and simulated ozone columns is the highest at 11–12%. However, ozone concentration variability in this layer,

which includes the tropopause where periodic flows of ozone-rich stratospheric air into the troposphere are observed, is also at its maximum at 35–40%. The SOCOL model significantly underestimates the measured data (by 12.9%), whereas the EMAC model underestimates it only slightly (by 1.5%). Due to the high variability of ozone content in this layer, the correlation coefficient between the experimental and modeled data is high and the same for both models (0.95), whereas the EMAC d value (0.97) is higher than that of SOCOLv3 (0.93), consistent with the smaller bias of EMAC.

Table 4. The statistical characteristics of the comparison between FTIR measurements and model simulations (SOCOLv3 and EMAC) in the vicinity of St. Petersburg from 2009 to 2019. The confidence intervals are given at the 95% significance level. R—correlation coefficient, *d*—Willmott index of agreement, CI—confidence interval.

Trace Gas	Days	SOCOL				EMAC			
		Bias, %	SDD, %	R	d (95% CI)	Bias, %	SDD, %	R	d (95% CI)
O_3	709	+0.1 ± 0.3	4.1	0.96 ± 0.02	0.980 (0.976–0.983)	−2.1 ± 0.3	4.0	0.96 ± 0.02	0.976 (0.971–0.979)
O_3 (8–18 km)	709	+12.9 ± 0.9	11.6	0.95 ± 0.02	0.934 (0.922–0.945)	+1.5 ± 0.9	11.8	0.95 ± 0.02	0.967 (0.959–0.974)
O_3 (18–25 km)	709	−2.6 ± 0.7	8.8	0.86 ± 0.04	0.91 (0.90–0.92)	−2.2 ± 0.5	7.2	0.91 ± 0.03	0.946 (0.939–0.952)
O_3 (25–60 km)	709	+0.3 ± 0.5	6.8	0.86 ± 0.04	0.92 (0.91–0.93)	−5.5 ± 0.7	9.6	0.70 ± 0.05	0.75 (0.73–0.77)
HNO_3	657	+20 ± 2	20	0.60 ± 0.06	0.60 (0.58–0.63)	+17 ± 1	16	0.81 ± 0.04	0.70 (0.68–0.72)
HCl	744	+11.6 ± 0.7	9.1	0.77 ± 0.05	0.73 (0.70–0.75)	+26.0 ± 0.6	7.6	0.91 ± 0.03	0.52 (0.50–0.54)
$ClONO_2$	633	+6.5 ± 4.5	57	0.61 ± 0.06	0.63 (0.58–0.68)	+3.0 ± 4.2	53	0.71 ± 0.06	0.70 (0.64–0.74)

In the middle stratosphere (18–25 km), both models slightly exceed the measured values, with the EMAC model agreeing somewhat better with the measured data (SDD of 7.2% versus 8.8%). In the upper stratosphere (25–60 km), where ozone concentration variability is primarily determined by photochemical reactions of formation and destruction, the SOCOL model agrees better with the measured data than the EMAC model. The relative errors (RE) are 6.8% and 9.6%, and the R values are 0.86 and 0.70, respectively. Additionally, the EMAC model overestimates the measured data by 5.5%, while no systematic differences are observed between the SOCOL simulations and the measurements. Moreover, in the 25–60 km layer, SOCOLv3 shows a higher *d* value (0.92) than EMAC (0.75), together with a lower SDD and a higher correlation coefficient, indicating closer overall agreement with the observations in this layer.

Overall, in the middle and upper stratosphere, the discrepancy between measurements and modeling is close to the 6–8% error margin of FTIR measurements in these layers [67], whereas in the lower stratosphere, the discrepancy exceeds the measurement uncertainty.

For other stratospheric trace gases, both models overestimate the observations: for HCl and HNO_3, up to 20–26%, and SDDs exceed the measurement errors to varying degrees (see Table 1). For HNO_3, the Willmott index is moderate for both models and is higher for EMAC than for SOCOLv3 (0.70 and 0.60, respectively), consistent with the higher correlation and lower SDD obtained for EMAC. For HCl, however, the two statistics provide different information: EMAC has a substantially higher correlation coefficient than SOCOLv3 (0.91 versus 0.77), indicating a closer correspondence in temporal variability, whereas the Willmott index is lower for EMAC (0.52 versus 0.73). This difference is associated with the substantially larger systematic bias of EMAC (26.0%) compared with SOCOLv3 (11.6%). For $ClONO_2$, EMAC provides both a higher R (0.71 versus 0.61) and d values (0.70 versus 0.63) than SOCOLv3, although the large SDD values indicate substantial discrepancies in the magnitude of the observed variability.

The authors of [65] analyzed previous versions of EMAC and SOCOL models in comparison with FTIR measurements of HCl and $ClONO_2$ TCs at 17 NDACC sites. In this study, SDDs with FTIR $ClONO_2$ data equaled 91% and 23% for EMAC and SOCOL models, respectively; with HCl data, they equaled 8% and 14%, respectively. In the current study, both models are much more consistent with experimental data for these gases.

Overall, the comparison of R, SDD, Bias, and d indicates that the relative agreement of the two models depends on the trace gas and atmospheric layer considered. EMAC generally provides a better description of the temporal variability of HNO_3, HCl, and $ClONO_2$, as reflected by higher correlation coefficients, whereas the Willmott index also reveals the influence of systematic bias on the overall agreement between simulations and observations.

3.2.2. Seasonal Cycle and Trend Estimates

Figure 8 illustrates the seasonal variations in ozone and ozone-related gases TCs, as derived from FTIR measurements and modeling. The seasonal variations were obtained using the method described in [36]. This method is effective for data presented on an irregular time grid and when there are long gaps in the data due to a lack of measurements, such as those caused by instrument malfunctions.

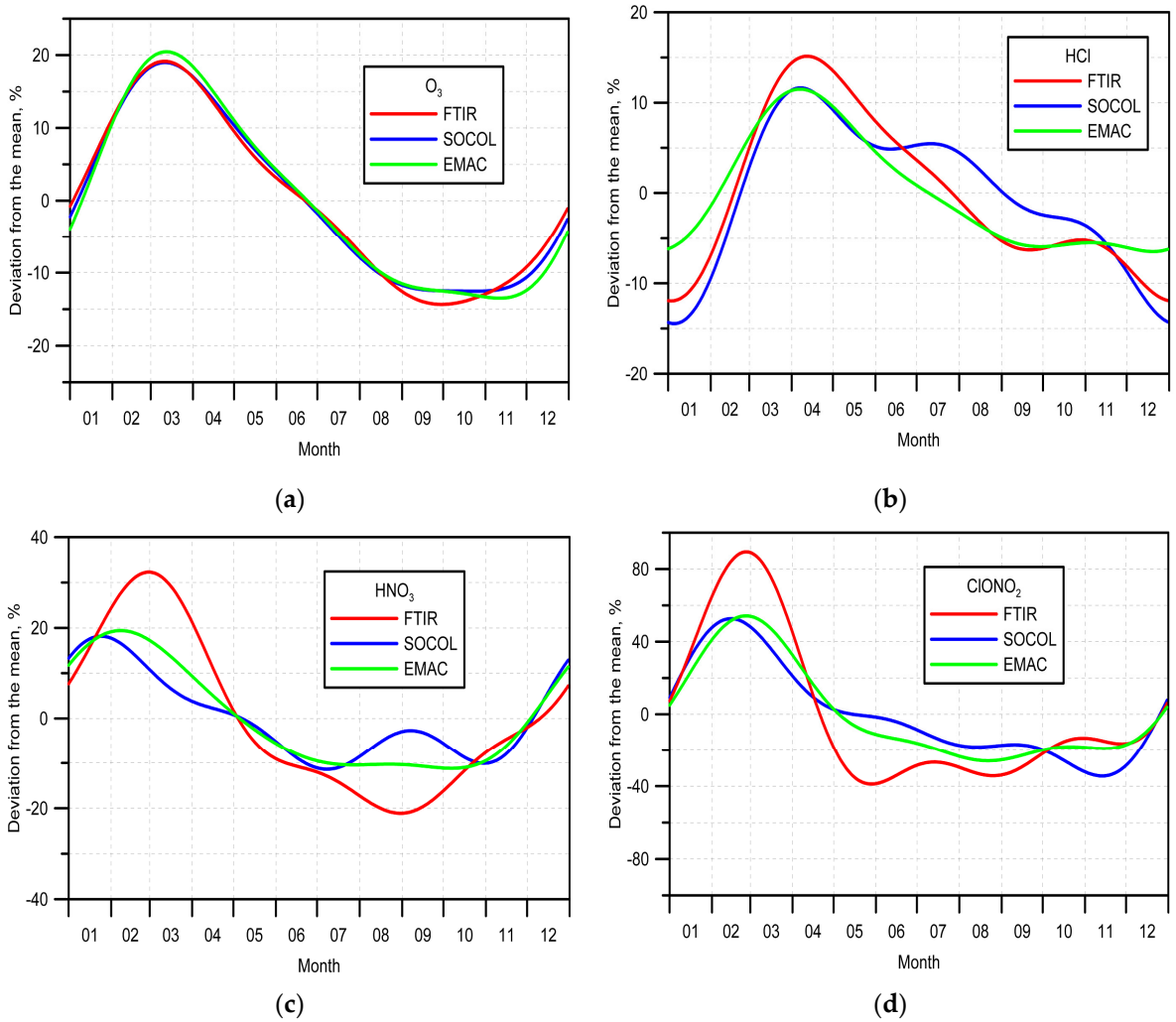


Figure 8. Seasonal variations in O_3 (**a**), HCl (**b**), HNO_3 (**c**), and $ClONO_2$ (**d**) TCs relative to the mean with the linear trend subtracted, derived from FTIR measurements and modeling at the SPbU site for the period from 2009 to 2019.

Both models reproduce the main seasonal pattern of the TOC. The agreement is generally better during spring, whereas larger discrepancies are observed in fall and early winter, when the number of FTIR measurements is smaller. This limited sampling increases the uncertainty of the seasonal-cycle estimate during these periods.

Both models yield similar values in the spring when describing seasonal variations in HCl TCs but diverge during the rest of the year. The SOCOLv3 model better describes the observed variations at the SPbU site in winter, while the EMAC model yields results closer to the experimental data in fall. At the peak, the amplitude of the variation in the measurements is greater than in the model data. Moreover, the peak in the model occurs about a week earlier than in the FTIR data. Additionally, the SOCOL model shows an additional peak in midsummer that is not observed in the measurement data or the EMAC model simulations.

A similar shift in the spring maximum and an additional summer feature have previously been reported for the SOCOLv2 model at several subarctic NDACC stations [65]. This comparison is included only to place the seasonal behavior identified in the present SOCOLv3 simulations in the context of earlier model versions and independent high-latitude observations. The EMAC model also better reproduces the seasonal variation in HCl in this study.

The maximum seasonal variation is significantly more pronounced in the experimental data than in the simulated data for the HNO_3 and $ClONO_2$ components. The EMAC and SOCOLv2 models also underestimated the seasonal variation in $ClONO_2$ at the geographically closest subarctic NDACC stations, Kiruna and Harestua [65]. In addition to having lower peak values, the peaks in both models describing the seasonal variation in HNO_3 occur nearly a month earlier than the IR measurement data. The SOCOL model exhibits a pronounced secondary peak at the end of summer that is absent in the EMAC model. The experimental data show a minimum at this time.

Overall, the observed seasonal pattern is reproduced least accurately for HNO_3 among the gases considered.

The seasonal differences for all gases complement the full-period statistical evaluation presented in Table 4 and the annual trend comparison in Table 5. Because of the uneven seasonal sampling, we do not provide separate seasonal values of bias, SDD, and R; instead, the seasonal differences are discussed qualitatively in conjunction with the quantitative full-period statistics in Table 4.

Table 5. Trend estimates of ozone and ozone-related gases obtained from FTIR measurements and numerical simulations near St. Petersburg for the 2009–2019 period. Statistically significant estimates at the 95% confidence level are in bold.

Target Gas	Trend, % yr^{-1}		
	FTIR	SOCOL	EMAC
O_3	+0.17 ± 0.26	+0.24 ± 0.24	+0.20 ± 0.21
O_3 (8–18 km)	+0.06 ± 0.62	+0.58 ± 0.59	+0.40 ± 0.53
O_3 (18–25 km)	+0.26 ± 0.27	**+0.43 ± 0.29**	**+0.34 ± 0.23**
O_3 (25–60 km)	+0.18 ± 0.23	−0.04 ± 0.20	+0.02 ± 0.17
HNO_3	−0.21 ± 0.48	**+0.49 ± 0.40**	**+0.69 ± 0.33**
$ClONO_2$	**−2.6 ± 1.5**	**−1.6 ± 0.6**	**−1.2 ± 0.5**
HCl	−0.04 ± 0.30	**+1.54 ± 0.24**	**−0.48 ± 0.33**

Table 5 shows trend estimates based on measurement and model simulations in the St. Petersburg area from 2009 to 2019. A comparison of the data in Table 2, which presents trend estimates based on FTIR measurements from 2009 to 2026, with the data in Table 5, which presents the same measurements but from 2009 to 2019, reveals that over the shorter period,

there is no statistically significant trend in ozone content across the three stratospheric layers. However, over the longer period, a statistically significant negative trend is evident in the lower and middle stratosphere and a positive trend in the upper stratosphere. These results may indicate a change in the stratospheric dynamics in the mid- and high latitudes of the Northern Hemisphere for specific years during the observation period. This change is reflected in the ozone content of the stratospheric layers, particularly the decrease in ozone during winter and spring in 2022, 2023, and 2025 (see Figure A1 in Appendix A.1).

Overall, trend estimates based on model data align well with those based on observational data. No statistically significant trend was observed in the lower or upper stratosphere during the 2009–2019 period. However, the model data show a consistent, statistically significant positive trend in the middle stratosphere (18–25 km). FTIR measurements for this layer also show a positive trend, though it is not statistically significant.

Estimates of linear trends in ozone content in various atmospheric layers derived from EMAC model simulations from 2002 to 2019 showed a statistically significant increase in ozone content in all three layers ($+0.26 \pm 0.10\%\ yr^{-1}$, $+0.18 \pm 0.04\%\ yr^{-1}$, and $+0.05 \pm 0.04\%\ yr^{-1}$ in the lower, middle, and upper stratosphere, respectively) and in the TOCs of $+0.14 \pm 0.04\%\ yr^{-1}$. Comparing these estimates with those in Table 5 reveals a shift in trends before and after 2009, particularly a slower rate of ozone layer recovery near St. Petersburg.

A statistically significant trend is observed only for the $ClONO_2$ TCs in both the numerical simulations and observations, and the trend estimates are consistent within the confidence interval. Additionally, both models indicate a statistically significant increase in HNO_3 TCs, which is not evident in the observations. The trend estimates for HCl differ substantially between the two models, with SOCOLv3 showing an increase ($+1.54 \pm 0.24\%\ yr^{-1}$) and EMAC showing a decrease ($-0.48 \pm 0.33\%\ yr^{-1}$). The present analysis does not allow this difference to be uniquely attributed to chemical or transport processes because no dedicated sensitivity experiments were performed. The discrepancy may reflect differences in the representation of atmospheric chemistry and transport, as well as differences in the meteorological forcing used by the two simulations.

The seasonal dependence of the model–observation relationship was evaluated separately from the long-term trend estimates using the seasonal-cycle analysis presented in Figure 8 for the common 2009–2019 period. The seasonal differences between the models and FTIR observations indicate that model performance varies throughout the year. However, because the observations are unevenly distributed in time and the number of measurements is particularly limited in some seasons, separate seasonal or monthly linear trend estimates would be associated with larger sampling uncertainty. We therefore retain the annual trend estimates in Table 5 and use Figure 8 to characterize the seasonal differences in model–observation behavior.

3.2.3. Short-Term Variability

In addition to evaluating the overall quality of the modeling, examining how models can describe individual episodes of short-term variability in stratospheric gases is also of interest.

Detailed results on ozone and related gas variability in the St. Petersburg area for winter and spring 2014 are reported in [35]. This analysis considered satellite data and available ground-based FTIR measurements. According to reanalysis data and HF TC measurements (see Appendix B.1 for details), there were periods when the atmosphere over St. Petersburg was potentially influenced by the PSV and there were days when chemical ozone losses were observed.

To analyze the state of the ozone layer over St. Petersburg, ERA5 reanalysis data on PSV and temperature at a pressure level of 50 hPa (corresponding to altitudes of 20–25 km, where PSCs form) were used [60]. When the temperature drops below 195 K, conditions arise for the formation of type I PSC particles and consequently for heterogeneous reactions involving them [21].

A significant temperature increase may indicate the onset of a sudden stratospheric warming event, which can substantially alter stratospheric circulation and influence the transport of ozone between the stratosphere and troposphere [82]. Consequently, changes in ozone content may result from changes in the transport and mixing of ozone-rich and ozone-poor air masses.

Figure 9 shows the temporal variability of ozone (Figure 9a), HCl (Figure 9b), HNO_3 (Figure 9c), and $ClONO_2$ (Figure 9d) obtained from FTIR measurements and modeling in the vicinity of St. Petersburg in March and April of 2014. The FTIR data are presented only for cloud-free days, whereas the model simulations are presented for each day. For clarity, the measurement data points are connected by a dashed line. However, it should be noted that there may be other values between measurements. Therefore, the comparison should be restricted to the days on which measurements were available.

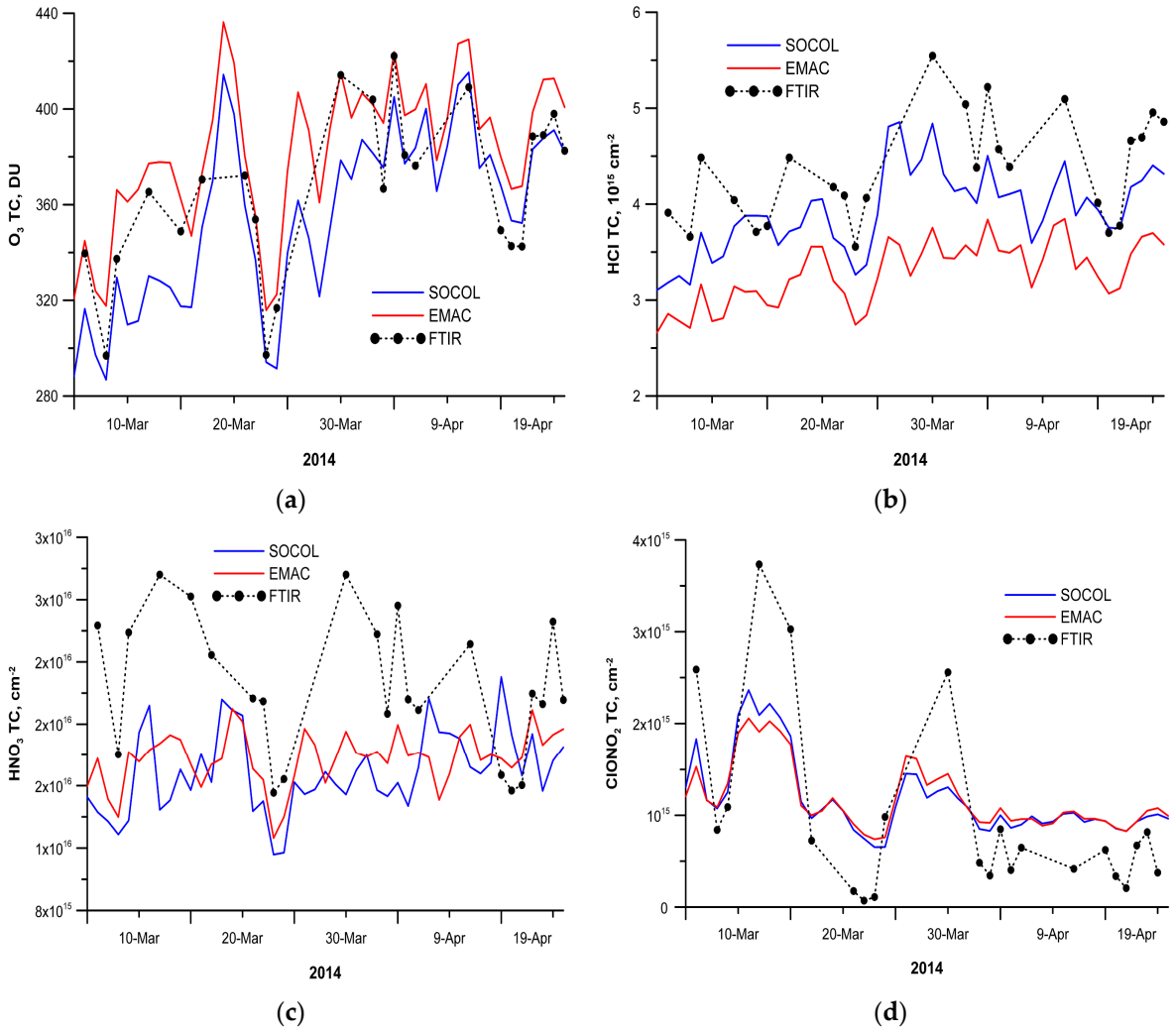


Figure 9. Time series of O_3 (**a**), HCl (**b**), HNO_3 (**c**), and $ClONO_2$ (**d**) TCs derived from FTIR measurements and modeling at the SPbU site in spring 2014.

In March 2014, the ratios of HCl and $ClONO_2$ to HF were out of phase (see Appendix B.1 and [35] for details). During this time, the variability of HNO_3 TCs as-

sociated with chemical reactions correlated with the variability of HCl TCs. Between 8 and 20 March, St. Petersburg was under the influence of PSV (see Appendix B.1) and an increase in $ClONO_2$ TCs associated with the deactivation of chlorine was observed. The decrease in HNO_3 TCs at that time may be associated with the photolysis of these molecules [4,21], which results in the formation of NO_2 molecules that neutralize ClO molecules during the $ClONO_2$ formation reaction. From March 20 to 25, a rapid rise in stratospheric temperature was accompanied by an increase in O_3, HCl and HNO_3 TCs and a simultaneous decrease in $ClONO_2$ TCs, which may be due to the mixing of polar and mid-altitude air masses. This may have been caused by the decomposition of $ClONO_2$ molecules due to photolysis and a greater relative contribution of the HCl formation reaction [21]. In late March and early April, the polar vortex approaches St. Petersburg again, causing a sharp decrease in stratospheric temperature and HNO_3 TCs. It is possible that some molecules transition from the gas phase to the solid phase, resulting in gravitational deposition.

To quantify the model–observation agreement during the March–April 2014 episode, the bias, SDD, correlation coefficient, and standard deviations of the FTIR and modeled time series were calculated using only the days on which FTIR observations were available. The number of paired observations was 27 for O_3, 27 for HNO_3, 28 for HCl, and 26 for $ClONO_2$. For O_3, the EMAC and SOCOLv3 models yielded biases of −4.0% and +2.5%, SDDs of 2.7% and 4.0%, and correlation coefficients of 0.96 and 0.91, respectively. The standard deviations of the observed and modeled O_3 columns were 32.5, 30.7, and 34.3 DU for FTIR, EMAC, and SOCOLv3, respectively.

For HCl, the EMAC and SOCOLv3 biases were +25.1% and +10.6%, with SDDs of 7.6% and 6.9% and correlation coefficients of 0.91 and 0.88, respectively. The standard deviations of the FTIR, EMAC, and SOCOLv3 HCl columns were 6.16×10^{14}, 3.46×10^{14}, and 4.53×10^{14} cm^{-2}, respectively. For HNO_3, the corresponding biases were +20.0% and +27.8%, SDDs were 16.2% and 23.1%, and correlation coefficients were 0.53 and −0.09. The standard deviations of the FTIR, EMAC, and SOCOLv3 HNO_3 columns were 4.28×10^{15}, 1.95×10^{15}, and 2.57×10^{15} cm^{-2}, respectively.

For $ClONO_2$, the correlation coefficients were high for both models (0.94 for EMAC and 0.93 for SOCOLv3), whereas the SDDs were 73.7% and 68.5%, respectively. The corresponding biases were −16.6% and −14.1%. The standard deviations of the FTIR, EMAC, and SOCOLv3 $ClONO_2$ columns were 9.51×10^{14}, 2.96×10^{14}, and 3.58×10^{14} cm^{-2}, respectively, indicating that both models substantially underestimate the amplitude of the observed $ClONO_2$ variability.

These quantitative results support the qualitative comparison shown in Figure 9. Both models reproduce the short-term variability of O_3, although EMAC shows a somewhat higher correlation with the observations. For HCl, both models reproduce the temporal pattern well, but the modeled variability is lower than that observed by FTIR. The EMAC model reproduces the temporal variability of HNO_3 better than SOCOLv3, whereas the SOCOLv3 correlation is close to zero. For $ClONO_2$, both models reproduce the temporal pattern with high correlation coefficients; however, the much smaller modeled standard deviations and large SDD values indicate that the amplitude of the observed variability is not adequately reproduced.

It should be noted that the model grid-cell value corresponding to the SPbU station represents a spatially averaged atmospheric state over a model grid cell of approximately $2.8^\circ \times 2.8^\circ$, whereas ground-based FTIR observations have a substantially smaller and geometry-dependent spatial sensitivity. Consequently, the model–observation comparison is not a strict point-to-point comparison. Differences may reflect both model errors and spatial representativeness differences, especially during synoptic events associated with strong horizontal gradients or localized ozone anomalies.

A detailed case study of intraday TOC variability on 27 March 2019 and its representation in the model simulations is presented in Appendix B.2.

4. Conclusions

This study provides an integrated analysis of ozone and ozone-related stratospheric trace gases over St. Petersburg using long-term ground-based FTIR observations from June 2009 to May 2026, complemented by harmonized FTIR and UV/VIS DOAS total ozone measurements. The analysis considers long-term trends, seasonal variability, rapid intraday changes, and chemistry-climate model evaluation.

Over the 2009–2026 observational period, statistically significant negative ozone trends were detected in the 8–18 km and 18–25 km layers, while no statistically significant long-term trend was detected for the total ozone column. Decreases in HNO_3 and several chlorine-containing species were also observed, together with an increase in upper-stratospheric ozone. The interpretation of these long-term changes indicates an important contribution from both stratospheric dynamics and changes in ozone-depleting substances.

The combination of FTIR and harmonized DOAS observations enabled the investigation of rapid intraday total ozone changes that cannot be resolved from FTIR measurements alone. The 27 March 2019 episode, selected because it exhibited the greatest intraday TOC variability in the FTIR record, demonstrated the importance of rapid air-mass transport for local ozone variability.

The model–observation evaluation was restricted to the common 2009–2019 period. EMAC and SOCOLv3 reproduced the main temporal variability of total ozone and several ozone partial columns, although their performance differed between atmospheric layers and trace gases. The analysis of the March–April 2014 episode showed that the models generally reproduced the main temporal patterns but underestimated the amplitude of observed variability for several gases. For HCl, HNO_3 and $ClONO_2$, quantitative differences between simulations and FTIR observations remain larger than the corresponding measurement uncertainties for parts of the record.

The main limitations of the study are the uneven temporal sampling of solar FTIR observations, particularly the sparse winter measurements; the large uncertainty and limited availability of ClO retrievals; and the spatial representativeness mismatch between the model grid cells and ground-based observations. Future work should focus on improving winter and early-spring observational coverage, increasing the sensitivity and uncertainty characterization of ClO retrievals, extending harmonized multi-instrument observations, and evaluating higher-resolution or regional models during episodes of strong synoptic variability.

Author Contributions: Conceptualization, G.N. and Y.V.; methodology, G.N., Y.V., A.P. and E.R.; software, Y.V., A.P. and S.A.; validation, G.N., Y.V. and P.N.; formal analysis, G.N., Y.V. and P.N.; investigation, Y.V.; resources, E.R.; data curation, Y.V., V.Z., A.P., D.I., S.A. and O.K.; writing—original draft preparation, Y.V. and G.N.; writing—review and editing, Y.V., G.N., O.K., D.I., A.P., S.A. and V.Z.; visualization, Y.V., P.N. and G.N.; supervision, Y.V.; project administration, E.R.; funding acquisition, E.R., Y.V., G.N. and A.P. All authors have read and agreed to the published version of the manuscript.

Funding: This research was funded by Saint Petersburg State University under research project 124032000025-1.

Data Availability Statement: The EMAC data is available at https://doi.org/10.35097/qvax1z6c5j93zkty (accessed on 11 September 2026). The measurement data and the SOCOLv3 numerical simulations are available on request from the corresponding authors due to restrictions on public distribution of the data since St. Petersburg State University is the intellectual property owner of these data.

Acknowledgments: The authors thank Maria Makarova, the principal investigator of the SPbU NDACC IRWG site, and colleagues from the Department of Physics of Atmosphere of SPbU, Anatoly Poberovsky and Hamud Imhasin, for providing FTIR spectroscopic measurements. SOCOLv3 simulations have been performed on the SPbU cluster. Spectroscopic measurements were performed using equipment at the SPbU Resource Center "Geomodel": FTIR-spectrometer manufactured by Bruker Optics GmbH & Co. KG (Germany), UV and VIS-spectrometers manufactured by Ocean Optics (USA).

Conflicts of Interest: The authors declare no conflicts of interest.

Abbreviations

The following abbreviations are used in this manuscript:

CCM	Chemical Climate Model
CFC	Chlorofluorocarbons
CI	Confidence Interval
DOAS	Differential Optical Absorption Spectroscopy
dofs	Degrees of Freedom for Signal
ECHAM	ECMWF Hamburg
ECMWF	European Centre for Medium-Range Weather Forecasts
EMAC	ECHAM/MESSy Atmospheric Chemistry
ERA	European Centre for Medium-Range Weather Forecasts, ReAnalysis
FTIR	Fourier Transform Infrared
HITRAN	HIgh-resolution TRANsmission
IR	Infrared
IRWG	Infrared Working Group
MA-ECHAM	Middle Atmosphere ECHAM
MESSy	Modular Earth Submodel System
MEZON	Model for the Evaluation of oZONe trends
NCEP CPC	Climate Prediction Center of the National Centers for Environmental Prediction
NDACC	Network for the Detection of Atmospheric Composition Change
PSC	Polar Stratospheric Cloud
PSV	Polar Stratospheric Vortex
PV	Potential Vorticity
RE	Relative Error
SD	Standard Deviation
SDD	Standard Deviation of Differences
SOC	Surface Ozone Concentrations
SOCOL	SOlar Climate Ozone Links
SPbU	St. Petersburg State University
SZA	Solar Zenith Angle
TC	Total Column
TOC	Total Ozone Column
TrOC	Tropospheric Ozone Column
UV	Ultraviolet
VIS	Visible
WACCM	Whole Atmosphere Community Climate Model

Appendix A

Appendix A.1. Time Series of Ozone and Ozone-Related Gases Measured by FTIR Method at SPbU Site

Figure A1 shows the time series of the measured daily average ozone total and partial columns and related trace-gas total columns obtained at the SPbU observational site from 2009 to 2026. The total number of valid FTIR measurement days for the individual gases

is given in Table 1. The observations are unevenly distributed throughout the year, with substantially more measurements obtained in spring and summer than in winter. The seasonal distribution of valid measurement days for each gas is summarized in Table A1. For example, for O_3, 123 observations were available in winter, 376 in spring, 309 in summer, and 149 in autumn.

The FTIR observations cover the period from June 2009 to May 2026, with measurements available on average for approximately 70 days per year. The observations are unevenly distributed throughout the year, with most measurements obtained during spring and summer and substantially fewer observations during winter due to the requirements of solar observations and local observing conditions (see Table A1). No FTIR measurements were available in 2024 because of instrumental problems (laser failure) with the Bruker IFS 125HR spectrometer. Due to solar tracking system failure, little data was obtained in 2020 and 2022. These temporal gaps and the uneven seasonal sampling should be considered when interpreting the seasonal variability and long-term trends.

Stratospheric gases (O_3, HNO_3, $ClONO_2$, and HCl) exhibit a pronounced seasonal pattern, peaking in the spring except for ozone columns in 25–60 km due to dynamical [79] and photochemical factors [4]; however, the seasonal pattern is less pronounced for CFCs (CFC-11 and CFC-12), peaking in the summer [36].

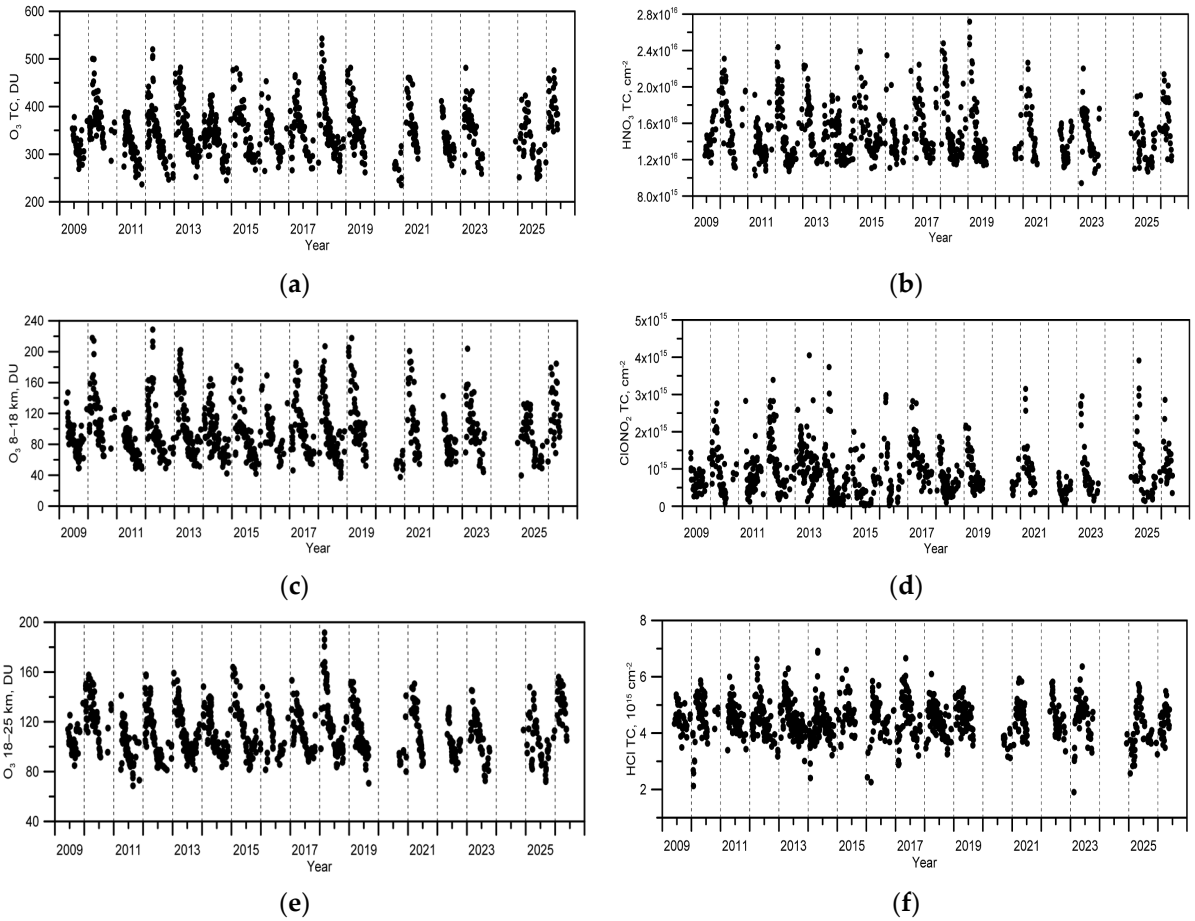


Figure A1. *Cont.*

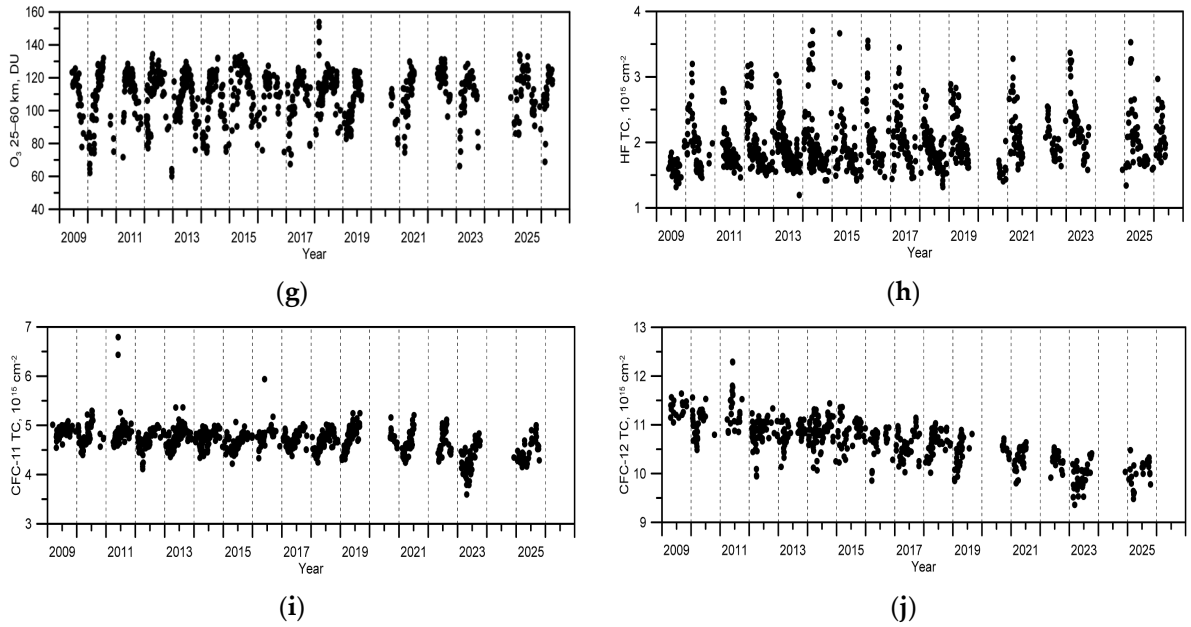


Figure A1. Time series of trace gases total and partial columns: O_3 TC (**a**), HNO_3 TC (**b**), O_3 8–18 km (**c**), $ClONO_2$ TC (**d**), O_3 18–25 km (**e**), HCl TC (**f**), O_3 25–60 km (**g**), HF (**h**), CFC-11 (**i**), and CFC-12 (**j**) measured by FTIR method near St. Petersburg in 2009–2026.

It is well seen that during the spring very high values of stratospheric gases, especially $ClONO_2$, can be observed. This corresponds to various dynamical processes in winter–spring stratosphere–tropopause movements and intrusion of PSV into mid-latitudes. HF TC levels allow distinguishing the variability of stratospheric gases due to dynamical reasons from chemical processes. In [83], indicators were used to determine the location of an air mass inside or outside the PSV at the Kiruna subpolar station (67.8° N) in the NDACC network during the winter/spring of 2001. The HF TCs and the ratio of COF_2 TC to HF TC were considered alongside the potential vorticity (PV) value at a potential temperature of 475 K. Despite significant correlations between HF TCs and PV values in other years, the study showed that, in the year under consideration, the air mass may be located within the PSV at low PV values (less than 3 K·m^2/kg·s). This is more accurately determined by the HF TC value when it exceeds 2.5 × 10^{15} cm^{-2}. This value was recommended as the criterion for determining whether an air mass is located at the edge of the PSV. As Figure A1h shows, the observed HF TCs exceed this value almost every spring.

Table A1. Number of valid FTIR measurement days for individual trace gases by season during 2009–2026. Winter: December–February, Spring: March–May, Summer: June–August, Autumn: September–November.

Target Gas	Total	Winter	Spring	Summer	Autumn
O_3	957	123	376	309	149
HNO_3	894	123	366	260	145
$ClONO_2$	837	107	351	245	134
HCl	1006	121	416	324	145
HF	1076	126	433	347	170
CFC-11	908	106	370	286	146
CFC-12	595	92	263	119	118

Appendix A.2. Trend Estimate of Trace Gas Columns Related to HF Total Columns

In the Northern Hemisphere, dynamic processes typically dominate the evolution of ozone concentration in the Arctic and adjacent regions (see, for example, [23]). To

isolate changes in trace gas concentrations attributable to dynamics from chemical reasons for subsequent analysis, the total and stratospheric columns of trace gases studied were normalized to the TCs of HF. Vertical profiles of the mixing ratio of ozone-layer trace gases generally correlate well with the HF profile in the lower stratosphere, where most of these trace gases are concentrated. Thus, vertical movements in the stratosphere change proportionally for both HF and other trace gases [84]. An increase in the HF TCs of 100%, which is associated with adiabatic subsidence in winter and spring, results in a 6% decrease in the ozone-to-HF TC ratio, an 11% decrease in the total HCl-and-$ClONO_2$-to-HF TC ratio, and a 20% decrease in the HNO_3-to-HF TC ratio. Meanwhile, a change in the tropospheric boundary layer height of several kilometers has virtually no effect on these ratios [85].

In addition to trend estimates discussed in Section 3.1.2, we evaluate time series of ozone and ozone-related stratospheric gases related to HF TCs. Table A2 presents the estimated trends of ozone and ozone-related stratospheric gases ratioed to HF TCs. As expected, the statistically significant negative trends in atmospheric gases shown in Table 2 have intensified due to the increase in HF TCs observed over the period under consideration.

Table A2. Trend estimates of ratio of ozone and ozone-related gases measured in different atmospheric layers to HF TCs at SPbU site by FTIR method from June 2009 to May 2026.

Target Gas	Layer, km	Trend, % yr^{-1}
O_3/HF	0–60	-0.44 ± 0.27
	18–25	-0.54 ± 0.30
HNO_3/HF	0–60	-0.65 ± 0.20
	15–60	-0.67 ± 0.18
$ClONO_2$/HF	0–60	-1.4 ± 0.7
HCl/HF	0–60	-0.77 ± 0.16
Cly/HF	0–60	-0.89 ± 0.16

Estimates of long-term trends in the trace gas-to-HF TC ratio can be useful for analyzing short-term variability in stratospheric gases, such as inter- or intra-annual variability, as well as for analyzing trend estimates across seasons, which are characterized by distinct chemical and photochemical reactions. For instance, the average ratio of HNO_3 to HF decreases gradually from late fall to spring due to the photolysis of HNO_3 molecules. Meanwhile, the average ratio of O_3 to HF depends on heterogeneous reactions when the air mass is inside the PSV [86]. Preliminary subtraction of long-term trends in the ratio of stratospheric gas columns to HF TCs improves the accuracy of the results analysis obtained.

Appendix B

Appendix B.1. Case Study: Stratospheric Dynamics in Spring 2014

Figure A2 illustrates the temporal evolution of the HF TC oscillation, as measured at the SPbU site alongside the PV, derived from ERA5 reanalysis data [60], at a potential temperature of 475 K for spring 2014. The solid line for PV indicates the edge of PSV [87], while the dashed line separates air masses inside PSV [88]. The HF TC value correlates well with the PV value. A study [35] shows that the correlation between PV and HF TC values was 0.58 ± 0.05 during the 2009–2019 measurement period. Since PV is typically determined and analyzed at only one atmospheric level, using HF TC values as a dynamic factor is more justified. HF TC maxima are characteristic of air masses located within the PSV. Thus, in March–April 2014, three periods of possible PSV intrusion into the air masses over St. Petersburg were observed.

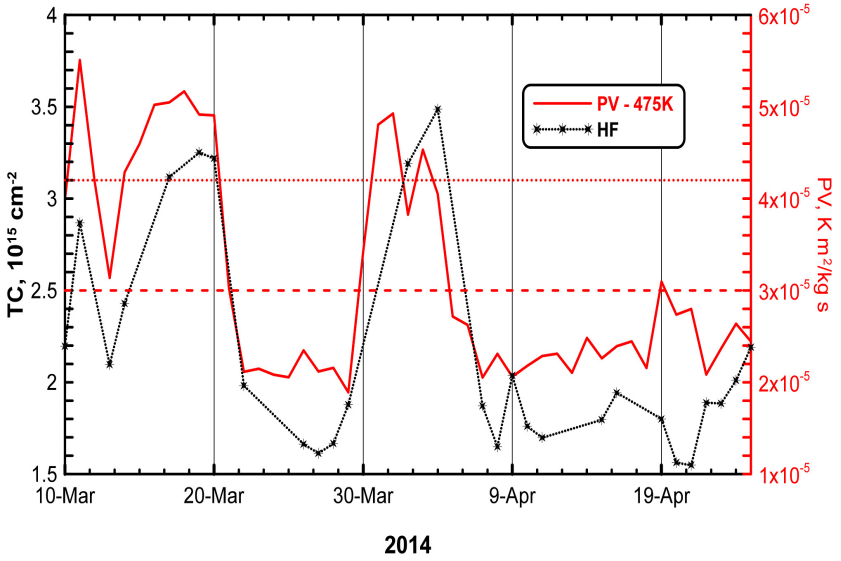


Figure A2. Time series of PV at 475 K potential temperature (ERA5 data) and HF TCs obtained from the FTIR measurements at the SPbU observational station in Peterhof in 2014.

According to the ERA5 reanalysis, during the period under consideration (March–April 2014), the temperature at 50 hPa remained above 195 K throughout. Only on March 10–12 did it approach the threshold for PSC particle formation [35]. The maximum PV value (5.6 K·m^2/kg·s) at 475 K was recorded on March 11. From March 8 to 13 and from March 30 to April 4, the air masses over St. Petersburg were on the edge of the PSV. From March 14 to 20, the air masses were inside the PSV. During this period, two instances of minor sudden stratospheric warming events (not accompanied by a significant change in zonal wind direction) were also observed over St. Petersburg. During these events, the stratospheric temperature rose by 20–25 degrees over the course of several days, from March 12 to 26. All these features can influence the stratospheric trace gas variability over St. Petersburg.

Appendix B.2. Case Study: Trace Gas Variability on 27 March 2019

In Section 3.1.4, nine days with pronounced diurnal TOC variability were identified (Table 3). Among these cases, 27 March 2019 was selected for detailed analysis using ERA5 analysis data because it exhibited the greatest diurnal variability in TOC based on the FTIR measurements. The purpose of this analysis is to illustrate a particularly pronounced short-term variability event and to examine its representation in the model simulations; it is not intended to provide a statistically representative assessment of all high-variability episodes.

The reanalysis data showed that the variability of TOC at the site was caused by dynamic processes, specifically active air mass transport—the replacement of air masses at the station containing varying amounts of ozone. Since the simulation data has a temporal resolution of one hour, we were able to analyze the intraday variability of ozone and related gases based on simulation and measurement data. We could also assess the quality of the model's ability to reproduce diurnal gas variability.

Figure A3 shows the intraday variation in O_3 (Figure A3a), HCl (Figure A3b), HNO_3 (Figure A3c), and $ClONO_2$ (Figure A3d) based on ground-based FTIR measurements at the SPbU site and numerical calculations from the EMAC and SOCOL models. Ground-based solar FTIR measurements do not provide continuous 24 h observations because measurements require direct solar radiation and are therefore restricted to daylight and cloud-free conditions. Consequently, Figure A3 should be interpreted as a comparison of intraday variability during the available daytime observation period rather than as a

complete 24 h diurnal cycle. The hourly model output is shown continuously, whereas the observational points are available only during suitable daylight measurement conditions.

The EMAC model shows greater intraday variability in O_3 for HNO_3 and $ClONO_2$ than the SOCOL model. However, for HCl, the opposite is true. The SOCOL model shows greater intraday variability in TCs. Both models describe the variability of O_3 similarly; however, the SOCOL model consistently yields higher TOC values than the EMAC model. For $ClONO_2$, however, the EMAC model yields higher TC values than the SOCOL model.

Overall, the simulation data show a smoothed trend in trace gas TC changes for all the gases considered. The data fail to capture the sharp changes observed during the second half of the day. This suggests that the models need further refinement to describe and predict rapid changes in ozone and related gases, including dynamic processes. Additionally, the smoother trend observed in the simulation data may be related to the models' spatial resolution, which, despite being tied to the SPbU site, is 2.8 by 2.8 degrees, meaning they present an average picture of a large area.

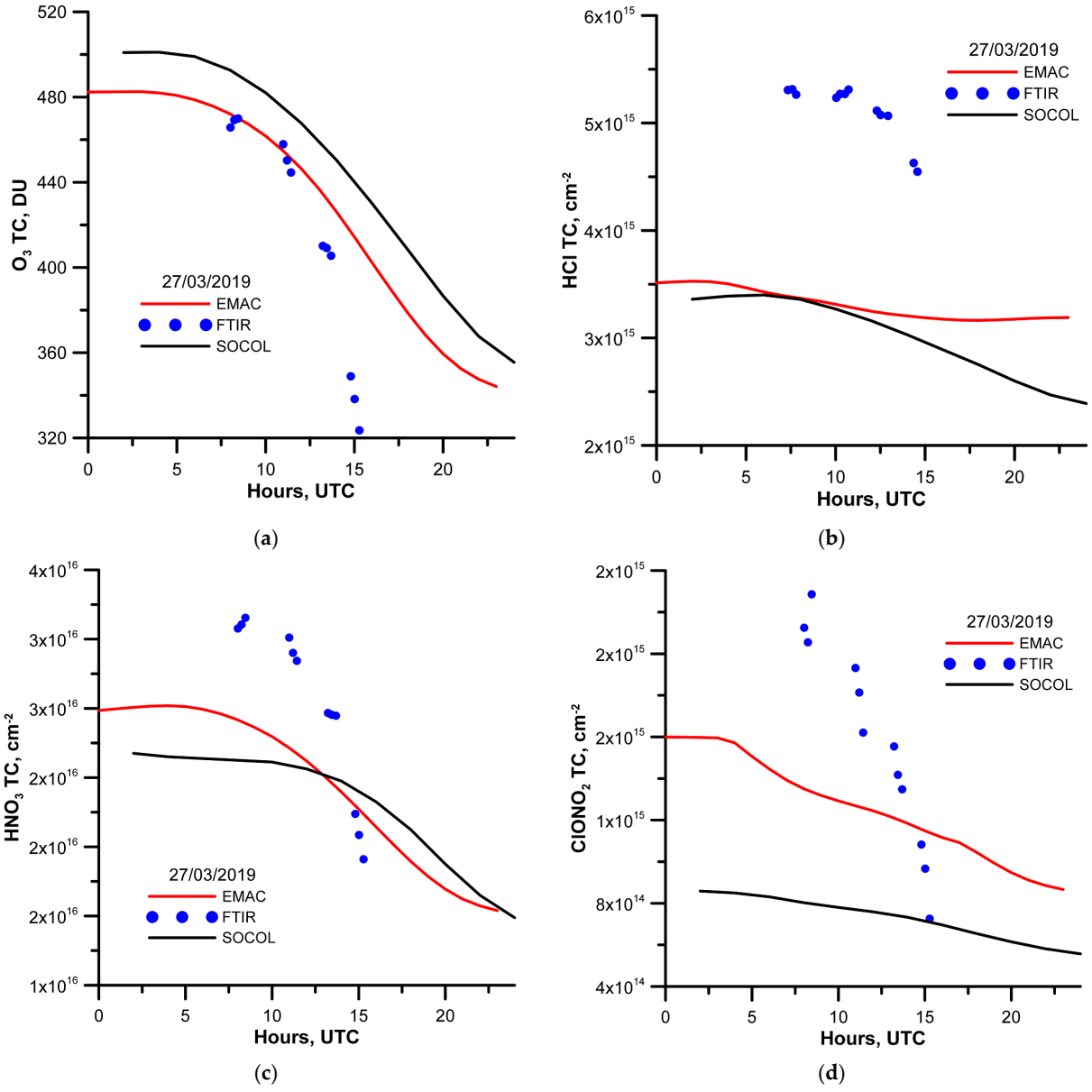


Figure A3. Intraday variability of O_3 (**a**), HCl (**b**), HNO_3 (**c**), and $ClONO_2$ (**d**) TCs derived from FTIR measurements and modeling at the SPbU site on 27 March 2019.

References

1. Müller, R. A brief history of stratospheric ozone research. *Meteorol. Z.* **2009**, *18*, 3–24. [CrossRef] [PubMed]
2. WMO. Scientific Assessment of Ozone Depletion: 2022—GAW Report No. 278. Available online: https://library.wmo.int/viewer/58360/download?file=2022OzoneAssessment.pdf&type=pdf&navigator=1 (accessed on 20 December 2025).
3. Larin, I. *Chemical Physics of the Ozone Layer*; LAP LAMBERT Academic Publishing: Saarbrücken, Germany, 2018; p. 264.
4. Seinfeld, J.H.; Pandis, S.N. *Atmospheric Chemistry and Physics: From Air Pollution to Climate Change*, 3rd ed.; John Wiley & Sons, Inc.: Hoboken, NJ, USA, 2016; p. 1152.
5. Bernhard, G.H.; Fioletov, V.E.; Grooß, J.U.; Ialongo, I.; Johnsen, B.; Lakkala, K.; Manney, G.L.; Müller, R.; Svenby, T. Record-Breaking Increases in Arctic Solar Ultraviolet Radiation Caused by Exceptionally Large Ozone Depletion in 2020. *Geophys. Res. Lett.* **2020**, *47*, e2020GL090844. [CrossRef] [PubMed]
6. Bowman, H.; Turnock, S.; Bauer, S.E.; Tsigaridis, K.; Deushi, M.; Oshima, N.; O'Connor, F.M.; Horowitz, L.; Wu, T.; Zhang, J.; et al. Changes in anthropogenic precursor emissions drive shifts in the ozone seasonal cycle throughout the northern midlatitude troposphere. *Atmos. Chem. Phys.* **2022**, *22*, 3507–3524. [CrossRef]
7. Chipperfield, M.P.; Bekki, S. Opinion: Stratospheric ozone—Depletion, recovery and new challenges. *Atmos. Chem. Phys.* **2024**, *24*, 2783–2802. [CrossRef]
8. Tuck, A.F. Perspective on aircraft in the stratosphere: 50 years from COMESA through the ozone hole to climate. *Q. J. R. Meteorol. Soc.* **2021**, *147*, 713–727. [CrossRef]
9. Crutzen, P.J. The influence of nitrogen oxides on the atmospheric ozone content. *Q. J. R. Meteorol. Soc.* **1970**, *96*, 320–325. [CrossRef]
10. Johnston, H. Reduction of stratospheric ozone by nitrogen oxide catalysts from supersonic transport exhaust. *Science* **1971**, *173*, 517–522. [CrossRef] [PubMed]
11. Stolarski, R.S.; Cicerone, R.J. Stratospheric Chlorine: A Possible Sink for Ozone. *Can. J. Chem.* **1974**, *52*, 1610–1615. [CrossRef]
12. Molina, M.; Rowland, F.S. Stratospheric sink for chlorofluoromethanes: Chlorine atom-catalysed destruction of ozone. *Nature* **1974**, *249*, 810–812. [CrossRef]
13. Bourguet, S.; Stone, K.; Lickley, M. Semi-empirical estimates of stratospheric circulation and the lifetimes of chlorofluorocarbons and carbon tetrachloride. *Commun. Earth Environ.* **2025**, *6*, 531. [CrossRef]
14. Sturrock, G.A.; Etheridge, D.M.; Trudinger, C.M.; Fraser, P.J.; Smith, A.M. Atmospheric histories of halocarbons from analysis of Antarctic firn air: Major Montreal Protocol species. *J. Geophys. Res.* **2002**, *107*, 4765. [CrossRef]
15. Ball, W.T.; Alsing, J.; Mortlock, D.J.; Staehelin, J.; Haigh, J.D.; Peter, T.; Tummon, F.; Stübi, R.; Stenke, A.; Anderson, J.; et al. Evidence for a continuous decline in lower stratospheric ozone offsetting ozone layer recovery. *Atmos. Chem. Phys.* **2018**, *18*, 1379–1394. [CrossRef]
16. Fleming, E.L.; Newman, P.A.; Liang, Q.; Daniel, J.S. The impact of continuing CFC-11 emissions on stratospheric ozone. *J. Geophys. Res. Atmos.* **2020**, *125*, e2019JD031849. [CrossRef]
17. Reimann, S.; Western, L.M.; Lickley, M.J.; Sherry, D.; Daniel, J.S.; Kuijpers, L.J.M.; Montzka, S.A.; Rigby, M.; Velders, G.J.M.; Vollmer, M.K.; et al. Continuing industrial emissions are delaying the recovery of the stratospheric ozone layer. *Nat. Commun.* **2026**, *17*, 3190. [CrossRef] [PubMed]
18. von Clarmann, T. Chlorine in the stratosphere. *Atmósfera* **2013**, *26*, 415–458. [CrossRef]
19. Toumi, R.; Jones, R.L.; Pyle, J.A. Stratospheric ozone depletion by $ClONO_2$ photolysis. *Nature* **1993**, *365*, 37–39. [CrossRef]
20. Kumar, A.; Karami, K.; Jacobi, C. A 45-year climatological study of arctic stratospheric polar vortex dynamics and morphology using ERA5 data (1979–2023). *Clim. Dyn.* **2025**, *63*, 403. [CrossRef]
21. Solomon, S. Stratospheric ozone depletion: A review of concepts and history. *Rev. Geophys.* **1999**, *37*, 275–316. [CrossRef]
22. Schoeberl, M.R.; Hartmann, D.L. The dynamics of the stratospheric polar vortex and its relation to springtime ozone depletions. *Science* **1991**, *251*, 46–52. [CrossRef] [PubMed]
23. Balis, D.S. An update on the dynamically induced episodes of extreme low ozone values over the northern middle latitudes. *Int. J. Remote Sens.* **2011**, *32*, 9197–9205. [CrossRef]
24. Khosrawi, F.; Kirner, O.; Sinnhuber, B.-M.; Johansson, S.; Höpfner, M.; Santee, M.L.; Froidevaux, L.; Ungermann, J.; Ruhnke, R.; Woiwode, W.; et al. Denitrification, dehydration and ozone loss during the 2015/2016 Arctic winter. *Atmos. Chem. Phys.* **2017**, *17*, 12893–12910. [CrossRef]
25. Manney, G.L.; Livesey, N.J.; Santee, M.L.; Froidevaux, L.; Lambert, A.; Lawrence, Z.D.; Millán, L.F.; Neu, J.L.; Read, W.G.; Schwartz, M.J.; et al. Record-Low Arctic Stratospheric Ozone in 2020: MLS Observations of Chemical Processes and Comparisons with Previous Extreme Winters. *Geophys. Res. Lett.* **2020**, *47*, e2020GL089063. [CrossRef]
26. Solomon, S.; Haskins, J.; Ivy, D.J.; Min, F. Fundamental Differences Between Arctic and Antarctic Ozone Depletion. *Proc. Natl. Acad. Sci. USA* **2014**, *111*, 6220–6225. [CrossRef] [PubMed]
27. Vargin, P.; Smyshlyaev, S.; Guryanov, V.; Chubarova, N.; Ionov, D.; Bankova, T.; Ivanova, N.; Solomatnikova, A. A Study of the Low-Ozone Episode over Scandinavia and Northwestern Russia in March 2025. *Atmosphere* **2025**, *16*, 1033. [CrossRef]

28. Karagodin-Doyennel, A.; Rozanov, E.; Sukhodolov, T.; Egorova, T.; Sedlacek, J.; Peter, T. The future ozone trends in changing climate simulated with SOCOLv4. *Atmos. Chem. Phys.* **2023**, *23*, 4801–4817. [CrossRef]
29. Oreskes, N.; Shrader-Frechette, K.; Belitz, K. Verification, validation, and confirmation of numerical models in the Earth sciences. *Science* **1994**, *263*, 641–646. [CrossRef] [PubMed]
30. De Mazière, M.; Thompson, A.M.; Kurylo, M.J.; Wild, J.D.; Bernhard, G.; Blumenstock, T.; Braathen, G.O.; Hannigan, J.W.; Lambert, J.-C.; Leblanc, T.; et al. The Network for the Detection of Atmospheric Composition Change (NDACC): History, status and perspectives. *Atmos. Chem. Phys.* **2018**, *18*, 4935–4964. [CrossRef]
31. Petropavlovskikh, I.; De Mazière, M.; Thompson, A.M.; Wild, J.D.; Hannigan, J.W.; Selkirk, H.B.; Hannun, R.A.; Steinbrecht, W.; Lambert, J.-C.; Van Malderen, R.; et al. Overview: The Network for the Detection of Atmospheric Composition Change at 35 years: Achievements and future strategy. *Atmos. Chem. Phys.* **2026**, *26*, 8637–8675. [CrossRef]
32. Timofeyev, Y.; Virolainen, Y.; Makarova, M.; Poberovsky, A.; Polyakov, A.; Ionov, D.; Osipov, S.; Imhasin, H. Ground-based spectroscopic measurements of atmospheric gas composition near Saint Petersburg (Russia). *J. Mol. Spectrosc.* **2016**, *323*, 2–14. [CrossRef]
33. NDACC. Network for the Detection of Atmospheric Composition Change. Available online: https://ndacc.larc.nasa.gov/ (accessed on 20 December 2025).
34. Chipperfield, M.P.; Burton, M.; Bell, W.; Paton Walsh, C.; Blumenstock, T.; Coffey, M.T.; Hannigan, J.W.; Mankin, W.G.; Galle, B.; Mellqvist, J.; et al. On the use of HF as a reference for the comparison of stratospheric observations and models. *J. Geophys. Res. Atmos.* **1997**, *102*, 12901–12919. [CrossRef]
35. Virolainen, Y.A.; Polyakov, A.V.; Timofeyev, Y.M. Analysis of the Variability of Stratospheric Gases Near St. Petersburg Using Ground-Based Spectroscopic Measurements. *Izv. Atmos. Ocean. Phys.* **2021**, *57*, 148–158. [CrossRef]
36. Polyakov, A.; Poberovsky, A.; Makarova, M.; Virolainen, Y.; Timofeyev, Y.; Nikulina, A. Measurements of CFC-11, CFC-12, and HCFC-22 total columns in the atmosphere at the St. Petersburg site in 2009–2019. *Atmos. Meas. Tech.* **2021**, *14*, 5349–5368. [CrossRef]
37. Virolainen, Y.; Polyakov, A.; Timofeyev, Y.; Poberovsky, A. FTIR Measurements of Stratospheric Gases at the St. Petersburg Site. In *Problems of Geocosmos—2022*; Kosterov, A., Lyskova, E., Mironova, I., Apatenkov, S., Baranov, S., Eds.; Springer Proceedings in Earth and Environmental Sciences; Springer: Cham, Switzerland, 2023. [CrossRef]
38. Akishina, S.; Polyakov, A.; Virolainen, Y. Ground-based measurements of HF and HCl total columns in atmosphere near Saint Petersburg (2009–2023). *Int. J. Remote Sens.* **2024**, *45*, 2315–2336. [CrossRef]
39. Virolainen, Y.; Nerobelov, G.; Polyakov, A.; Zubov, V.; Rozanov, E.; Imanova, A.; Akishina, S. Study of Ozone Variability over Russia by Means of Measurements and Modeling. *Atmosphere* **2026**, *17*, 265. [CrossRef]
40. Poberovskii, A.V. High-resolution ground measurements of the IR spectra of solar radiation. *Atmos. Ocean Opt.* **2010**, *23*, 161–163. [CrossRef]
41. Hase, H.; Hannigan, J.W.; Coffey, M.T.; Goldman, A.; Höpfner, M.; Jones, N.B.; Rinsland, C.P.; Wood, S.W. Intercomparison of retrieval codes used for the analysis of high-resolution, ground-based FTIR measurements. *J. Quant. Spectrosc. Radiat. Transf.* **2004**, *87*, 25–52. [CrossRef]
42. NSF National Center for Atmospheric Research (NCAR). Whole Atmosphere Community Climate Model (WACCM) Model Output ds313.6. Available online: https://gdex.ucar.edu/datasets/d313006/ (accessed on 20 December 2025).
43. Gordon, I.E.; Rothman, L.S.; Hargreaves, R.J.; Hashemi, R.; Karlovets, E.V.; Skinner, F.M.; Conway, E.K.; Hill, C.; Kochanov, R.V.; Tan, Y.; et al. The HITRAN 2020 molecular spectroscopic database. *J. Quant. Spectrosc. Radiat. Transf.* **2022**, *277*, 107949. [CrossRef]
44. Virolainen, Y.A.; Polyakov, A.V.; Kirner, O. Optimization of Procedure for Determining Chlorine Nitrate in the Atmosphere from Ground-Based Spectroscopic Measurements. *J. Appl. Spectrosc.* **2020**, *87*, 319–325. [CrossRef]
45. Virolainen, Y.A.; Ionov, D.V.; Polyakov, A.V. Analysis of Long-Term Measurements of Tropospheric Ozone at the St. Petersburg State University Observational Site in Peterhof. *Izv. Atmos. Ocean. Phys.* **2023**, *59*, 287–295. [CrossRef]
46. Virolainen, Y.A.; Timofeyev, Y.M.; Polyakov, A.V.; Poberovsky, A.V. Ground-Based FTIR Measurements of Atmospheric Nitric Acid at the NDACC St. Petersburg Site. *Izv. Atmos. Ocean. Phys.* **2023**, *59*, 167–173. [CrossRef]
47. Nerobelov, G.; Timofeyev, Y.; Virolainen, Y.; Polyakov, A.; Solomatnikova, A.; Poberovskii, A.; Kirner, O.; Al-Subari, O.; Smyshlyaev, S.; Rozanov, E. Measurements and Modelling of Total Ozone Columns near St. Petersburg, Russia. *Remote Sens.* **2022**, *14*, 3944. [CrossRef]
48. Rodgers, C.D. *Inverse Methods for Atmospheric Sounding: Theory and Practice*; World Scientific: Singapore, 2000. [CrossRef]
49. Rothman, L.S.; Gordon, I.E.; Barbe, A.; Benner, D.C.; Bernath, P.F.; Birk, M.; Boudon, V.; Brown, L.R.; Campargue, A.; Champion, J.-P.; et al. The HITRAN 2008 molecular spectroscopic database. *J. Quant. Spectrosc. Radiat. Transf.* **2009**, *110*, 533–572. [CrossRef]
50. Ionov, D.V.; Timofeyev, Y.M.; Poberovskii, A.V. Spectroscopic measurements of O_3 and NO_2 atmospheric content: Correction of ground-based method and comparison with satellite data. *Atmos. Ocean Opt.* **2015**, *28*, 526–532. [CrossRef]

51. Verhoelst, T.; Granville, J.; Hendrick, F.; Köhler, U.; Lerot, C.; Pommereau, J.-P.; Redondas, A.; Van Roozendael, M.; Lambert, J.-C. Metrology of ground-based satellite validation: Co-location mismatch and smoothing issues of total ozone comparisons. *Atmos. Meas. Tech.* **2015**, *8*, 5039–5062. [CrossRef]
52. WOUDC. World Ozone and Ultraviolet Radiation Data Centre. Available online: https://woudc.org/en/data/data-search-and-download (accessed on 20 December 2025).
53. Jöckel, P.; Kerkweg, A.; Pozzer, A.; Sander, R.; Tost, H.; Riede, H.; Baumgaertner, A.; Gromov, S.; Kern, B. Development cycle 2 of the Modular Earth Submodel System (MESSy2). *Geosci. Model Dev.* **2010**, *3*, 717–752. [CrossRef]
54. Roeckner, E.; Brokopf, R.; Esch, M.; Giorgetta, M.; Hagemann, S.; Kornblueh, L.; Manzini, E.; Schlese, U.; Schulzweida, U. Sensitivity of simulated climate to horizontal and vertical resolution in the ECHAM5 atmosphere model. *J. Clim.* **2006**, *19*, 3771–3791. [CrossRef]
55. Jöckel, P.; Sander, R.; Kerkweg, A.; Tost, H.; Lelieveld, J. Technical Note: The Modular Earth Submodel System (MESSy)—A new approach towards Earth System Modeling. *Atmos. Chem. Phys.* **2005**, *5*, 433–444. [CrossRef]
56. Dee, D.P.; Uppala, S.M.; Simmons, A.J.; Berrisford, P.; Poli, P.; Kobayashi, S.; Andrae, U.; Balmaseda, M.A.; Balsamo, G.; Bauer, P.; et al. The ERA-Interim reanalysis: Configuration and performance of the data assimilation system. *Q. J. R. Meteorol. Soc.* **2011**, *137*, 553–597. [CrossRef]
57. Stenke, A.; Schraner, M.; Rozanov, E.; Egorova, T.; Luo, B.; Peter, T. The SOCOL version 3.0 chemistry–climate model: Description, evaluation, and implications from an advanced transport algorithm. *Geosci. Model Dev.* **2013**, *6*, 1407–1427. [CrossRef]
58. Manzini, E.; Giorgetta, M.A.; Esch, M.; Kornblueh, L.; Roeckner, E. The influence of sea surface temperatures on the Northern winter stratosphere: Ensemble simulations with the MAECHAM5 model. *J. Clim.* **2006**, *19*, 3863–3881. [CrossRef]
59. Rozanov, E.V.; Zubov, V.A.; Schlesinger, M.E.; Yang, F.; Andronova, N.G. The UIUC 3-D Stratospheric Chemical Transport Model: Description and Evaluation of the Simulated Source Gases and Ozone. *J. Geophys. Res.* **1999**, *104*, 11755–11781. [CrossRef]
60. Hersbach, H.; Bell, B.; Berrisford, P.; Hirahara, S.; Horányi, A.; Muñoz-Sabater, J.; Nicolas, J.; Peubey, C.; Radu, R.; Schepers, D.; et al. The ERA5 global reanalysis. *Q. J. R. Meteorol. Soc.* **2020**, *146*, 1999–2049. [CrossRef]
61. Gardiner, T.; Forbes, A.; de Mazière, M.; Vigouroux, C.; Mahieu, E.; Demoulin, P.; Velazco, V.; Notholt, J.; Blumenstock, T.; Hase, F.; et al. Trend analysis of greenhouse gases over Europe measured by a network of ground-based remote FTIR instruments. *Atmos. Chem. Phys.* **2008**, *8*, 6719–6727. [CrossRef]
62. Sofieva, V.F.; Szelag, M.E.; Kramarova, N.A.; Damadeo, R.; Steinbrecht, W.; Petropavlovskikh, I.; Vigouroux, C.; Maillard Barras, E.; Zawada, D.; Tourpali, K.; et al. Updated global and regional trends of stratospheric ozone profiles. *Atmos. Chem. Phys.* **2026**, *26*, 7387–7405. [CrossRef]
63. Newman, P.A.; Lait, L.R.; Kramarova, N.A.; Coy, L.; Frith, S.M.; Oman, L.D.; Dhomse, S.S. Record High March 2024 Arctic Total Column Ozone. *Geophys. Res. Lett.* **2024**, *51*, e2024GL110924. [CrossRef]
64. Agel, L.; Cohen, J.; Barlow, M.; Pfeiffer, K.; Francis, J.; Garfinkel, C.I.; Kretschmer, M. Cold-air outbreaks in the continental US: Connections with stratospheric variations. *Sci. Adv.* **2025**, *11*, eadq9557. [CrossRef] [PubMed]
65. Kohlhepp, R.; Ruhnke, R.; Chipperfield, M.P.; De Mazière, M.; Notholt, J.; Barthlott, S.; Batchelor, R.L.; Blatherwick, R.D.; Blumenstock, T.; Coffey, M.T.; et al. Observed and simulated time evolution of HCl, $ClONO_2$, and HF total column abundances. *Atmos. Chem. Phys.* **2012**, *12*, 3527–3556. [CrossRef]
66. Yamanouchi, S.; Strong, K.; Colebatch, O.; Conway, S.; Jones, D.B.A.; Lutsch, E.; Roche, S. Atmospheric trace gas trends obtained from FTIR column measurements in Toronto, Canada from 2002–2019. *Environ. Res. Commun.* **2021**, *3*, 051002. [CrossRef]
67. Jonas, C.; Vigouroux, C.; Langerock, B.; Björklund, R.; Boynard, A.; Carlund, T.; De Mazière, M.; Effertz, P.; Errera, Q.; Frey, M.M.; et al. Detection of ozone recovery in the Arctic from ground-based measurements. *Atmos. Chem. Phys.* **2026**, *26*, 8089–8124. [CrossRef]
68. Raymond, N.; Bernath, P.; Boone, C.; Chipperfield, M.P. Twenty-One Years of Global Atmospheric Chlorine Inventories From Atmospheric Chemistry Experiment Fourier Transform Spectrometer (ACE-FTS) Measurements. *J. Geophys. Res. Atmos.* **2026**, *131*, e2025JD045176. [CrossRef]
69. Mahieu, E.; Chipperfield, M.; Notholt, J.; Reddmann, T.; Anderson, J.; Bernath, P.F.; Blumenstock, T.; Coffey, M.T.; Dhomse, S.S.; Feng, W.; et al. Recent Northern Hemisphere stratospheric HCl increase due to atmospheric circulation changes. *Nature* **2014**, *515*, 104–107. [CrossRef] [PubMed]
70. Chrysanthou, A.; Dubé, K.; Tegtmeier, S.; Chipperfield, M.P. Hemispheric Asymmetry in Stratospheric Trends of HCl and Ozone: Impact of Chemical Feedback on Ozone Recovery. *J. Geophys. Res. Atmos.* **2025**, *130*, e2024JD042161. [CrossRef]
71. Dubé, K.; Tegtmeier, S.; Bourassa, A.; Laube, J.C.; Engel, A.; Saunders, L.N.; Walker, K.A.; Hossaini, R.; Bednarz, E.M. Chlorinated very short-lived substances offset the long-term reduction of inorganic stratospheric chlorine. *Commun. Earth Environ.* **2025**, *6*, 487. [CrossRef]
72. Strahan, S.E.; Smale, D.; Douglass, A.R.; Blumenstock, T.; Hannigan, J.W.; Hase, F.; Jones, N.B.; Mahieu, E.; Notholt, J.; Oman, L.D.; et al. Observed hemispheric asymmetry in stratospheric transport trends from 1994 to 2018. *Geophys. Res. Lett.* **2020**, *47*, e2020GL088567. [CrossRef]

73. Schneider, M.; Hase, F.; Blumenstock, T.; Redondas, A.; Cuevas, E. Quality assessment of O_3 profiles measured by a state-of-the-art ground-based FTIR observing system. *Atmos. Chem. Phys.* **2008**, *8*, 5579–5588. [CrossRef]
74. Lindenmaier, R.; Batchelor, R.L.; Strong, K.; Fast, H.; Goutail, F.; Kolonjari, F.; McElroy, C.T.; Mittermeier, R.L.; Walker, K.A. An evaluation of infrared microwindows for ozone retrievals using the Eureka Bruker 125HR Fourier transform spectrometer. *J. Quant. Spectrosc. Radiat. Transf.* **2010**, *111*, 569–585. [CrossRef]
75. Antokhin, P.N.; Belan, B.D. Control of the dynamics of tropospheric ozone through the stratosphere. *Atmos. Ocean Opt.* **2013**, *26*, 207–213. [CrossRef]
76. Elansky, N.F.; Golitsyn, G.S.; Crutzen, P.J.; Belikov, I.B.; Brenninkmeijer, C.A.M.; Skorokhod, A.I. Observations of the Atmospheric Composition over Russia: TROICA Experiments. *Izv. Atmos. Ocean. Phys.* **2021**, *57*, 72–90. [CrossRef]
77. Seo, J.-H.; Cho, J.; Hong, E.; Cho, S.; Gil, J.; Joo, T.; Weon, S. Seasonally adaptive data-driven ozone prediction in megacity environments. *Environ. Res.* **2026**, *293*, 123741. [CrossRef] [PubMed]
78. Chen, Y.; Chen, D.; Nie, L.; Liu, W.; Fan, J.; Chen, X.; Zhang, Y. Seasonal predictability of the dominant surface ozone pattern over China linked to sea surface temperature. *npj Clim. Atmos. Sci.* **2024**, *7*, 17. [CrossRef]
79. Butchart, N. The Brewer-Dobson circulation. *Rev. Geophys.* **2014**, *52*, 157–184. [CrossRef]
80. Vigouroux, C.; De Mazière, M.; Demoulin, P.; Servais, C.; Hase, F.; Blumenstock, T.; Kramer, I.; Schneider, M.; Mellqvist, J.; Strandberg, A.; et al. Evaluation of tropospheric and stratospheric ozone trends over Western Europe from ground-based FTIR network observations. *Atmos. Chem. Phys.* **2008**, *8*, 6865–6886. [CrossRef]
81. OSCAR. Observing Systems Capability Analysis and Review Tool. Available online: https://space.oscar.wmo.int/ (accessed on 20 December 2025).
82. Lee, J.; Butler, A.H.; Albers, J.R.; Wu, Y.; Lee, S.H. Impact of Sudden Stratospheric Warmings on the Stratosphere-To-Troposphere Transport of Ozone. *Geophys. Res. Lett.* **2025**, *52*, e2024GL112588. [CrossRef]
83. Blumenstock, T.; Kopp, G.; Hase, F.; Hochschild, G.; Mikuteit, S.; Raffalski, U.; Ruhnke, R. Observation of unusual chlorine activation by ground-based infrared and microwave spectroscopy in the late Arctic winter 2000/01. *Atmos. Chem. Phys.* **2006**, *6*, 897–905. [CrossRef]
84. Toon, G.C.; Blavier, J.-F.; Sen, B.; Salawitch, R.J.; Osterman, G.B.; Notholt, J.; Rex, M.; McElroy, C.T.; Russell, J.M., III. Ground-based observations of Arctic O_3 loss during spring and summer 1997. *J. Geophys. Res.* **1999**, *104*, 26497–26510. [CrossRef]
85. Mellqvist, J.; Galle, B.; Blumenstock, T.; Hase, F.; Yashcov, D.; Notholt, J.; Sen, B.; Blavier, J.-F.; Toon, G.C.; Chipperfield, M.P. Ground-based FTIR observations of chlorine activation and ozone depletion inside the Arctic vortex during the winter of 1999/2000. *J. Geophys. Res. Atmos.* **2002**, *107*, 8263. [CrossRef]
86. Blumenstock, T.; Hase, F.; Kramer, I.; Mikuteit, S.; Fischer, H.; Goutail, F.; Raffalski, U. Winter to winter variability of chlorine activation and ozone loss as observed by ground-based FTIR measurements at Kiruna since winter 1993/94. *Int. J. Remote Sens.* **2009**, *30*, 4055–4064. [CrossRef]
87. Farahani, E.; Fast, H.; Mittermeier, R.L.; Makino, Y.; Strong, K.; Coffey, M.T.; Mikuteit, S.; Hase, F.; Blumenstock, T.; Raffalski, U.; et al. Nitric acid measurements at Eureka obtained in winter 2001–2002 using solar and lunar Fourier transform infrared absorption spectroscopy: Comparisons with observations at Thule and Kiruna and with results from three-dimensional models. *J. Geophys. Res. Atmos.* **2007**, *112*, D01305. [CrossRef]
88. Kopp, G.; Berg, H.; Blumenstock, T.; Fischer, H.; Hase, F.; Ruhnke, R.; Raffalski, U.; Kondo, Y. Evolution of ozone and ozone-related species over Kiruna during the SOLVE/THESEO 2000 campaign retrieved from ground-based millimeter-wave and infrared observations. *J. Geophys. Res. Atmos.* **2003**, *108*, SOL 51-1–SOL 51-12. [CrossRef]

Disclaimer/Publisher's Note: The statements, opinions and data contained in all publications are solely those of the individual author(s) and contributor(s) and not of MDPI and/or the editor(s). MDPI and/or the editor(s) disclaim responsibility for any injury to people or property resulting from any ideas, methods, instructions or products referred to in the content.